

## Compact intracloud lightning discharges:

### 1. Mechanism of electromagnetic radiation and modeling

Amitabh Nag<sup>1</sup> and Vladimir A. Rakov<sup>1</sup>

Received 19 March 2010; revised 14 June 2010; accepted 21 July 2010; published 20 October 2010.

[1] On the basis of experimental evidence of multiple reflections and modeling, we infer that, from the electromagnetic point of view, the so-called compact intracloud lightning discharge (CID) is essentially a bouncing-wave phenomenon. The shortest radiating-channel length appears to be about 100 m. Reflections, occurring at CID channel ends, influence the magnitude of the overall CID electric field waveform and are responsible for its fine structure, as well as, by inference, for “noisiness” of dE/dt waveforms and for accompanying HF-VHF bursts. From modeling the CID as a wave traveling on an elevated vertical transmission line and comparing model-predicted electric fields with measurements, we estimated that the effective current reflection coefficients at channel ends (additionally accounting for current attenuation along the channel) should be in the range of 0 to  $-0.5$ , that the wave propagation speed ranges from 0.3 to  $3 \times 10^8$  m/s, and the channel length is less than 1000 m. In these calculations, we assumed that the current wave had a zero-to-peak risetime of  $6 \mu\text{s}$  and a total duration of  $30 \mu\text{s}$ . Influence of current risetime on field waveforms was also examined, and it was found to be typically in the range from about 2 to  $8.5 \mu\text{s}$ .

**Citation:** Nag, A., and V. A. Rakov (2010), Compact intracloud lightning discharges: 1. Mechanism of electromagnetic radiation and modeling, *J. Geophys. Res.*, 115, D20102, doi:10.1029/2010JD014235.

#### 1. Introduction

[2] Compact Intracloud Discharges (CIDs) are cloud lightning discharges that produce single bipolar electric field pulses (sometimes referred to as Narrow Bipolar Pulses (NBPs) or Narrow Bipolar Events (NBEs)) having typical full widths of 10 to  $30 \mu\text{s}$  and intense HF-VHF radiation bursts (much more intense than those from any other cloud-to-ground or “normal” cloud discharge processes). These discharges were first reported by *Le Vine* [1980] and received their name, CID [Smith *et al.*, 1999], due to their inferred relatively small (hundreds of meters) spatial extent. Although CIDs have been studied for about three decades, they remain the most mysterious type of lightning, as evidenced by the following quotes. “Since we do not know the location, either in space within the storm or in time relative to any familiar lightning process, of the sources of these peculiar pulses [NBPs], it is perhaps premature to speculate on their nature....” [Willett *et al.*, 1989]. “The events are so different, in fact, that a novel type of discharge mechanism appears to be required in order to explain the observations....” [Smith *et al.*, 1999]. “Even if the breakdown mechanism is the same, with unobserved streamers or leaders preconditioning the air, NBE are still distinctly different from conventional lightning due to their impulsive

nature and very high peak RF power....” [Eack, 2004]. “The mechanism for producing a NBP is not yet known, but they are believed to be the most powerful natural terrestrial source of electromagnetic radiation in the HF and VHF radio bands....” [Watson and Marshall, 2007]. “A clear understanding of the meteorological setting of NBEs is still lacking....” [Wiens *et al.*, 2008]. “... it remains to be seen if NBPs have anything to do with the mechanism described in this [runaway electron avalanche] study....” [Dwyer *et al.*, 2009].

[3] Most of the reported electric field signatures of CIDs are produced by distant (tens to hundreds of kilometers) events and hence are essentially radiation [e.g., *Le Vine*, 1980; *Willett et al.*, 1989; *Smith et al.*, 1999, 2004], with only two close waveforms, which are dominated by the induction and electrostatic field components, being reported (one by *Eack* [2004] and one by *Nag et al.* [2010]). *Eack* [2004] reported both distant and close electric fields produced by the same CID. Both wideband electric and wideband magnetic field waveforms with accompanying VHF bursts produced by CIDs were observed by *Nag et al.* [2010]. *Watson and Marshall* [2007] used the original transmission line (TL) model [*Uman et al.*, 1975] and a modified TL model with an exponentially increasing current along the channel to compute CID electric field signatures at horizontal distances of a few and 200 km and compare them with corresponding measured waveforms reported by *Eack* [2004]. Both models can successfully match the two-station field measurements. The exponentially increasing current was assumed by *Watson and Marshall* to correspond

<sup>1</sup>Department of Electrical and Computer Engineering, University of Florida, Gainesville, Florida, USA.

to the runaway electron breakdown process. The original TL model was also employed by *Le Vine* [1980]. In all the modeling studies to date the TL was assumed to be energized at one end with the other end being terminated in its characteristic impedance, so that the traveling wave is totally absorbed there. A good agreement with measurements was achieved for currents and speeds comparable to those of return strokes in cloud-to-ground lightning; that is, for current peaks of some tens of kiloamperes, durations of some tens of microseconds, and speeds on the order of  $10^8$  m/s.

[4] In this paper, we propose a conceptual mechanism of CID electromagnetic radiation and present a bouncing-wave model based on this mechanism that allows reproduction of both overall observed electromagnetic field signatures of CIDs and their fine structure (if any). The physics of the CID channel and conditions under which it is formed are outside the scope of this paper. The model is used to determine “allowed” (consistent with experimental data) ranges of effective current reflection coefficients at channel ends, propagation speed, channel length, and current rise-time. Additionally, the Hertzian dipole approximation is considered, and the validity of both the bouncing-wave model and Hertzian dipole approximation is tested against two-station measurements of *Eack* [2004]. The “physics” sign convention according to which a downward directed electric field (or field change) vector is considered to be negative is used throughout the paper.

## 2. Experimental Setup and Data

[5] The data were acquired in summers of 2007 and 2008 in Gainesville, Florida, and include wideband electric fields, electric field derivatives (dE/dt), magnetic field derivatives (dB/dt), and narrowband VHF (36 MHz) radiation bursts produced by CIDs. For some events we also have narrowband HF (5 MHz) radiation records. A total of 220 CIDs were examined in this study. Phenomenological characteristics of 157 CIDs, including their occurrence context, dependence of electric field waveform on distance, source heights, normalized electric field peaks and other waveform parameters, acquired in August–September of 2008 in Gainesville, Florida, are presented by *Nag et al.* [2010].

[6] The electric field measuring system included an elevated circular flat-plate antenna followed by an integrator and a unity-gain, high-input-impedance amplifier. The system had a useful frequency bandwidth of 16 Hz to 10 MHz, the lower and upper limits being determined by the RC time constant (about 10 ms) of the integrator and by the amplifier, respectively. The electric field derivative (dE/dt) measuring system included an elevated circular flat-plate antenna followed by an amplifier. The magnetic field derivative (dB/dt) measuring system employed two orthogonal loop antennas (measuring two orthogonal components of dB/dt), each followed by an amplifier. The antennas were installed on the roof of a three-storey (in 2007) or a five-storey (in 2008) building in Gainesville, Florida. The upper frequency responses of the dE/dt and dB/dt measuring systems were 17 MHz and 15 MHz, respectively. The HF measuring system used an elevated circular flat-plate antenna and had its center frequency at 5 MHz with a  $-3$  dB bandwidth of 4.7 MHz to 5.4 MHz. The VHF measuring system used a whip antenna, and its center frequency was 36 MHz with a  $-3$  dB band-

width of 34 to 38 MHz. Fiber optic links were used to transmit the wideband field, field-derivative and HF signals from the antennas and associated electronics to an eight-bit digitizing oscilloscope. In the VHF system, a double-shielded and sleeved coaxial cable was used for this purpose. The oscilloscope digitized the signals at 100 MHz (10 ns sampling interval).

## 3. Evidence of Reflections in CID Electromagnetic Field Signatures

[7] *Hamlin et al.* [2007] reported that 12% of their CIDs each showed evidence of one current-pulse reflection, which appeared as a secondary pulse after the initial peak in their distant electric field waveforms. They interpreted the secondary pulse as a signature of reflection of the current pulse off the “far end” of the CID channel and used this feature to estimate CID channel lengths. The average time interval between the primary and secondary electric field peaks was  $6.7 \mu\text{s}$  with a standard deviation of  $2.7 \mu\text{s}$ . The upper bound on the channel length (determined assuming that the current wave traveled at the speed of light) was found to be about 2 km. In the following, we will present experimental evidence of multiple (up to 7) reflections from both ends of the CID channel. Our pulse detection efficiency was considerably higher than *Hamlin et al.*'s, because, in addition to electric fields, we measured electric field derivatives (dE/dt). By comparing our simultaneous electric field and dE/dt records, we found that *Hamlin et al.*'s secondary peak is likely to be a higher-order one, with the true first secondary peak and other lower-order secondary peaks being undetectable, and therefore would result in an overestimate if used for calculating radiator length. Also, from modeling, electric field peaks of the same polarity as that of the main pulse occur at the time when the current front is in the middle of the channel, in contrast with *Hamlin et al.*'s [2007] assumption that they occur at the time when the first reflection is produced at the far end of the channel.

[8] In Figure 1, we present wideband electric field (Figure 1a), dE/dt (Figure 1b), and VHF radiation burst (Figure 1c) produced by one of the CIDs in our data set. For this event, the initial polarity of wideband electric field waveform (see Figure 1a) is the same as that of negative return strokes and consistent with motion of positive charge upward (or negative charge downward), which is less common for CIDs. The duration, about  $16 \mu\text{s}$ , is typical for NBPs (10 to  $30 \mu\text{s}$  on average). A superposition of the wideband electric field, dE/dt, and VHF signatures is shown in Figure 1d. A more common event with initial electric field polarity consistent with motion of negative charge upward is shown in a similar format in Figure 2, with HF signature additionally presented in Figure 2c and VHF signature shown only in the superposition plot (Figure 2d). Both events occurred at unknown distances, but their wideband fields are clearly dominated by the radiation field component.

[9] At least one pronounced secondary peak (labeled S4) having the same polarity as the primary peak and multiple shoulders (labeled S1–S3 and S5) are seen after the primary peak in Figure 1a. We observed one or more secondary peaks in 34 (15%) of 220 CID electric field records, while in 186 (85%) cases no secondary peak could be identified. Following *Hamlin et al.* [2007], we measured time intervals

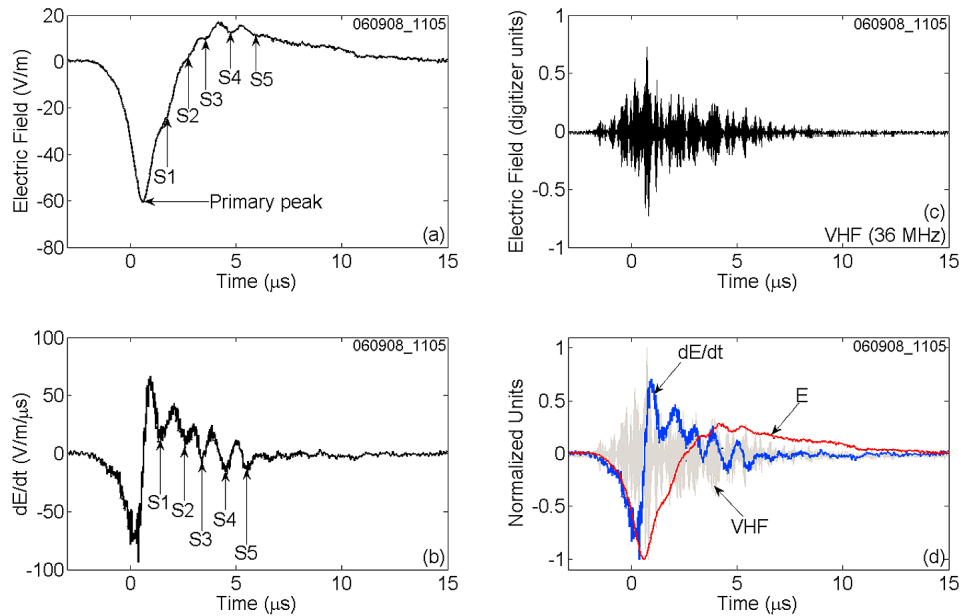


**Figure 1.** (a) Wideband electric field, (b)  $dE/dt$ , and (c) VHF radiation signatures of a CID that transferred negative charge downward (or positive charge upward), recorded in Gainesville, Florida. The event occurred at an unknown distance. (d) The three signatures overlaid for direct comparison. S1–S5 are five secondary peaks appearing as pronounced oscillations in Figure 1b and mostly as shoulders in Figure 1a. Electric field and  $dE/dt$  waveforms have been low-pass filtered to accentuate reflection signatures.

between the primary and first clear secondary peak (S4 in Figure 1a) of the same polarity in electric field records of 34 CIDs. They ranged between  $1.0 \mu\text{s}$  to  $5.8 \mu\text{s}$  with a mean of  $3.2 \mu\text{s}$ . The latter is about a factor of two shorter than Hamlin et al.'s mean of  $6.7 \mu\text{s}$ .

[10] In  $dE/dt$  signatures, secondary peaks (see Figure 1b) appear as pronounced oscillations after the initial opposite polarity (positive) overshoot. There are five pronounced cycles in Figure 1b, whose negative half cycles are labeled S1 to S5. The first three of them correspond to shoulders S1

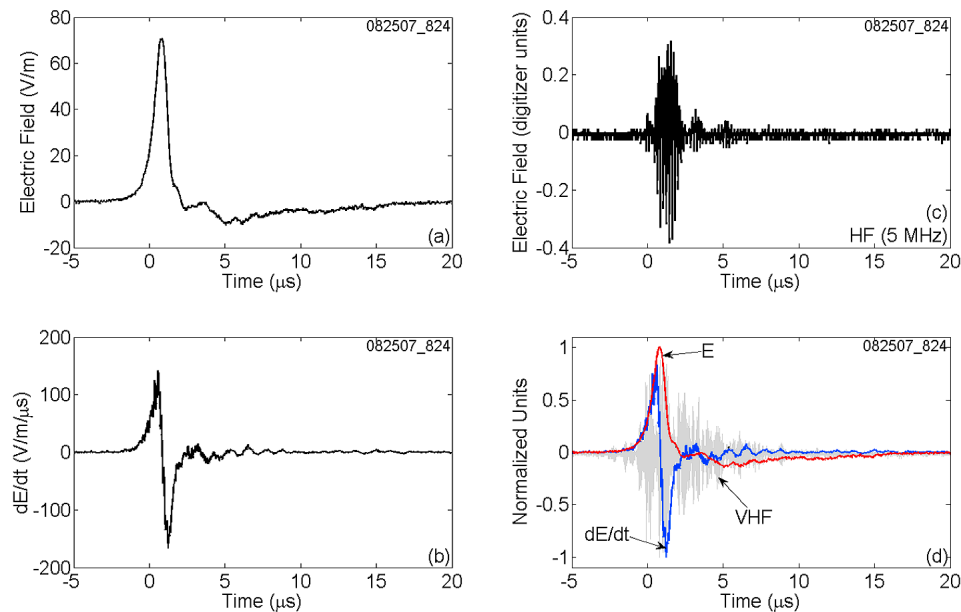


**Figure 2.** (a) Wideband electric field, (b)  $dE/dt$ , and (c) HF radiation signatures of a CID that transferred negative charge upward (or positive charge downward), recorded in Gainesville, Florida. The event occurred at an unknown distance. (d) Electric field,  $dE/dt$ , and HF signatures overlaid for direct comparison. Electric field and  $dE/dt$  waveforms have been low-pass filtered to accentuate reflection signatures.

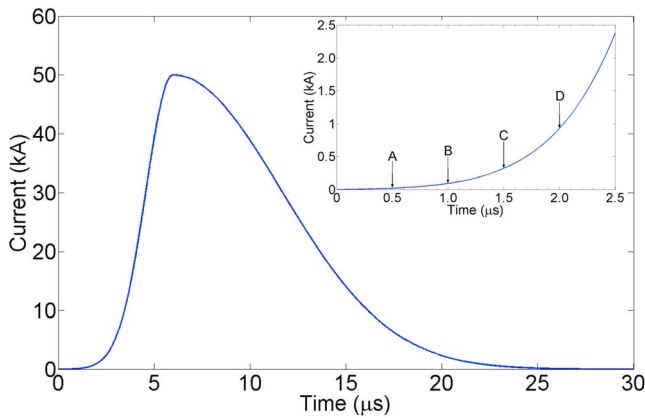


**Figure 3a.** A CID current pulse with a peak of 50 kA, total duration of 30  $\mu\text{s}$  and zero-to-peak risetime of 6  $\mu\text{s}$ , injected at the bottom of a 100 m long vertical conducting channel at  $t = 0$ . The inset shows the initial 2.5  $\mu\text{s}$  of the incident current waveform and times (see vertical arrows) at which the first four reflections begin. The wave makes two round trips (experiences four reflections) during the initial 2  $\mu\text{s}$ , six round trips (12 reflections) during the current risetime (6  $\mu\text{s}$ ), and 30 round trips (60 reflections) during the entire current duration (30  $\mu\text{s}$ ). In practice, due to attenuation along the channel and absorption at channel ends, higher-order reflections will be progressively less pronounced, so that less than 10 reflections are expected to be detectable in the  $dE/dt$  waveforms and even less in electric field signatures.

to S3 and the following one to the secondary peak S4 in Figure 1a. Note that peaks in electric field waveform correspond to local “zeros” in  $dE/dt$  waveform (and vice versa), as seen in Figure 1d where the two waveforms (as well as the VHF radiation signature) are superimposed. We found multiple secondary peaks (oscillations), which are indicative of reflections, in 32 (15%) of 212  $dE/dt$  records. We will show later that CID channel lengths are unlikely to exceed 1000 m. For this reason, we believe that partial reflections at channel ends should occur in the majority of CIDs, but may be undetectable even in  $dE/dt$  records. Factors that can make reflections undetectable include a relatively small magnitude of the incident wave, relatively long radiating channel, relatively large losses along the channel, and a relatively small (in absolute value) current reflection coefficients at channel ends. It is important to note that lower-order reflections (during the primary portion of the overall electric field or  $dE/dt$  waveform), while being undetectable, do influence the magnitude of the overall waveform (see Figure A2b). It is likely that (all other conditions being the same) the 15% of waveforms showing pronounced reflections correspond to shortest CID channels. The average time interval between consecutive peaks of the same polarity in  $dE/dt$  signatures ranged from 0.84 to 1.8  $\mu\text{s}$  (with a mean of 1.2  $\mu\text{s}$ ). We will show later, via modeling, that the multiple peaks (oscillations) in  $dE/dt$  waveforms can be produced by reflections at either end of CID channel, with the time interval between consecutive peaks (oscillation period) being equal to the roundtrip time along the channel. One half of the period is the channel traversal time. Interestingly, the period of

oscillations remains more or less constant (see Figure 1b), implying that the radiator length remains fixed during the bouncing-wave process and essentially ruling out the possibility that reflections are related to some discontinuities (e.g., branches or kinks) along the channel. A round trip time of 1  $\mu\text{s}$  corresponds, for example, to a propagation speed of  $2 \times 10^8$  m/s and a channel length of 100 m.

[11] In our data, the VHF signature usually begins at about the same time as the electric field and  $dE/dt$  signatures, and all three have comparable durations. In contrast, the corresponding HF signature in our data (see Figure 2c) began, on average, 1.7  $\mu\text{s}$  after the electric field,  $dE/dt$ , and VHF signatures did. An apparent delay in the onset of HF relative to VHF may be related to the production of longer streamers (associated with lower-frequency fields) at later times. There appears to be some structure in the VHF radiation waveforms in Figures 1c and 2d, but we could not uniquely relate this structure to features of corresponding electric field or  $dE/dt$  waveforms.

#### 4. Bouncing-Wave Mechanism

[12] On the basis of the evidence of multiple reflections, we postulate that, from the electromagnetic point of view, the compact intracloud discharge is essentially a bouncing-wave phenomenon. It can be viewed as beginning with injection of current pulse at one end of a relatively short conducting channel (this channel could be created by the runaway electron breakdown process [e.g., Tierney *et al.*, 2005, Gurevich and Zybin, 2004, Gurevich *et al.*, 2004]), which is reflected multiple times successively at either end of the channel until it is attenuated and absorbed, depending upon the conditions along the channel and boundary conditions at channel ends, respectively. The concept is illustrated by four schematic snapshots in Figure 3.

[13] Figure 3a shows a CID current pulse (similar to that inferred by Watson and Marshall [2007]) with a peak current of 50 kA, total duration of 30  $\mu\text{s}$  (much longer than expected time needed to traverse the channel), and zero-to-peak risetime of 6  $\mu\text{s}$  (somewhat shorter than 9  $\mu\text{s}$  in Watson and Marshall’s pulse, but more consistent with experimental data, as shown in Appendix B), injected at the bottom of a 100 m long vertical conducting channel at  $t = 0$ . The pulse ( $i_0$ ) travels upward at an assumed speed of  $2 \times 10^8$  m/s (similar to that inferred by Watson and Marshall [2007]), so that the front of this pulse will reach the top of the channel at  $t = 0.5 \mu\text{s}$ . The instant just before the pulse hits the top is schematically shown in segment A of Figure 3b. At the top of the channel, the current pulse in general will “see” an impedance discontinuity and hence will be partly reflected. The front of the current pulse (scaled according to the reflection coefficient at the top of the channel) will move downward. This is shown in segment B of Figure 3b. The downward motion of the current pulse front will continue till  $t = 1 \mu\text{s}$  at which time it will hit the bottom of the channel where it will be reflected again and begin traveling upward (segment C in Figure 2b). The second reflection at the top and resultant downward moving wave are depicted in segment D of Figure 3b. Note that while the initial parts of the current pulse front have already experienced multiple reflections at the top and bottom of the channel, later portions of the front (total front duration is 6  $\mu\text{s}$ ) are still making their

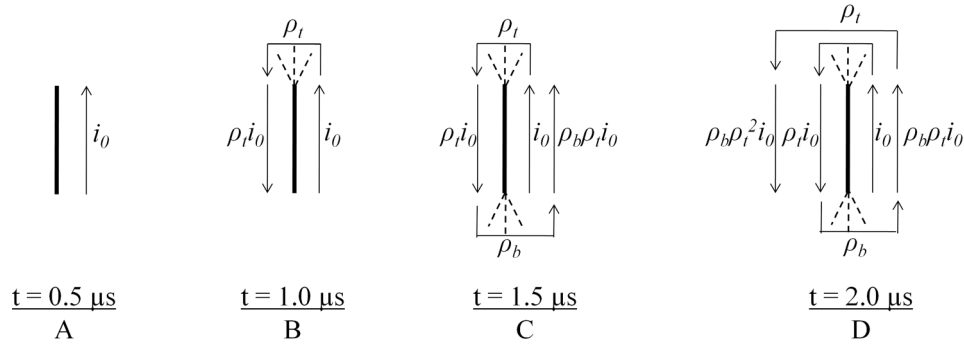


**Figure 3b.** Schematic representation of the bouncing-wave mechanism of CID for the case of channel length  $\Delta h = 100$  m and propagation speed  $v = 2 \times 10^8$  m/s. Current-wave duration is much longer than the channel traversal time. Straight arrows represent current waves on CID channel, and bracket-shaped arrows represent the process of wave reflection at the ends. If  $\rho_b = \rho_t = 1$  (short-circuit conditions), it is the same wave bouncing between the ends (folding on itself). If  $\rho_b = \rho_t = -1$  (open-circuit conditions), the wave changes polarity each time it hits the end. If  $\rho_b = \rho_t = -0.5$ , the current wave changes polarity and is reduced in magnitude by a factor of 2 at each end. If  $\rho_t = 0$ , the wave is fully absorbed at the top end. For  $|\rho_t| < 1$  and  $|\rho_b| < 1$ , partial absorption takes place at the top and bottom, respectively. It is expected that reflected current waves will reduce current at each end, while corresponding voltage will be enhanced there. As a result, corona-like electrical breakdown (shown by dashed lines) may occur at the channel ends. Breakdown associated with the incident wave,  $i_0$ , is not shown here.

first trip upward, or did not even emerge from the bottom of the channel. The process can be viewed as a long wave repeatedly folding on itself, so that the electromagnetic signature duration is not necessarily a measure of radiator length. At  $t = 30.5 \mu\text{s}$ , the last point on the tail of the originally injected current pulse will reach the top. After  $t = 0.5 \mu\text{s}$ , in addition to the upward-moving incident wave ( $i_0$ ), different portions of the pulse will be traveling either downward or upward after being reflected from the top or the bottom of the channel, respectively. However, with each successive reflection and traversal of the channel, the current pulse will be diminished due to partial absorption at the channel end and attenuation along the channel. The multiple current reflections are illustrated in Figure 3c where current reflection coefficients at the top ( $\rho_t$ ) and bottom ( $\rho_b$ ) of the channel were assumed to be equal to  $-1$  (open-circuit conditions).

[14] One of the features of CIDs is very strong HF-VHF radiation. It is generally thought that HF-VHF radiation is produced due to electrical breakdown of virgin air. The CID mechanism described above implies that HF-VHF radiation will be produced (1) when the front of current pulse moves upward along the channel for the first time and (2) at either end of the channel when current reflections are produced there. Reflections of different portions of current pulse may result in corona-like electrical breakdown (represented by dashed lines in Figure 3b) at channel extremities, because a reduction of current is accompanied by an increase of line charge density and associated voltage (voltage doubles at an open-circuit end and increases by a factor of 1.5 if the current reflection coefficient  $\rho = -0.5$ ). We speculate that the electric breakdown at both channel ends is likely to produce an intense burst of HF-VHF radiation which is a characteristic feature of CIDs (see Figures 1c, 2c and 2d). Further, the

proposed scenario can help explain the “noisiness” of  $dE/dt$  waveforms compared to corresponding electric field waveforms, a CID feature first noticed by *Willett et al.* [1989].

### 5. Bouncing-Wave Model: Current Distribution Along the Channel

[15] Let us consider a vertical channel whose bottom and top ends are at heights of  $h_1$  and  $h_2$ , respectively. The

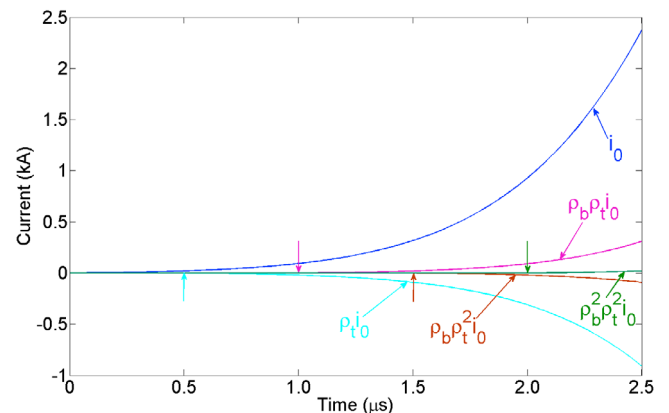


**Figure 3c.** Illustration of first four current reflections with reflection coefficients at the top ( $\rho_t$ ) and bottom ( $\rho_b$ ) of the channel assumed to be equal to  $-1$ . Times at which the reflections begin are marked with vertical arrows. Later reflections appear to diminish in magnitude because of later starting times.

assumption that the CID channel is generally vertical is supported by large magnitudes of the vertical component of electric field measured at ground level [see, e.g., *Willett et al.*, 1989; *Smith et al.*, 1999; *Nag et al.*, 2010] that are comparable with or exceeding those of first return strokes. The larger the deviation of the channel from vertical, the smaller the vertical component of electric field at ground level. For an essentially horizontally oriented channel this field component at ground level is close to zero. Additionally, the observed occurrence of CIDs between horizontally extensive charge layers [e.g., *Rison et al.*, 1999] and their relatively short channels are probably consistent with more or less vertical orientation. We do not consider here the process of creation of the CID channel. The presence of conducting channel in the cloud is evidenced by pronounced VLF/LF field waveforms. We assume that the channel is energized by injection of a current wave at its bottom end. According to the transmission line (TL) model that relates the longitudinal current  $i(z,t)$  at any height  $z$  and any time  $t$  to the current at the channel origin (which in our case is at  $h_1$ ),

$$i(z,t) = i\left(h_1, t - \frac{z - h_1}{v}\right). \quad (1)$$

In order to account for the multiple reflections that take place at the channel ends (as described in section 4) we specify two equivalent current sources,  $i_u(h_1,t)$  and  $i_d(h_2,t)$  (see Appendix A, equations (A1) and (A2)), connected at the bottom and at the top of the channel, respectively. Current  $i_u(h_1,t)$  accounts for the incident wave and all reflections at  $h_1$ ; it propagates upward. Current  $i_d(h_2,t)$  accounts for all reflections at  $h_2$  and propagates downward. One can compute partial electric fields at observation point P due to each of these two currents. The total electric field at P due to a current wave originating at  $h_1$  and undergoing multiple reflections at both channel ends is given by the superposition of these two electric field components (see Appendix A).

[16] Let us consider the event illustrated in Figure 3. A current pulse with a peak of 50 kA, total duration of 30  $\mu$ s, and zero-to-peak risetime of 6  $\mu$ s (see Figure 3a) is injected at the bottom of a 100 m long vertical channel. We assume that the bottom of the channel is at an altitude of 15 km [*Nag et al.*, 2010] and that negative charge is transferred upward. The pulse travels upward at an assumed speed of  $2 \times 10^8$  m/s. The round-trip time for the current pulse along the channel from bottom to top and back is 1  $\mu$ s. Let the current reflection coefficients at the bottom and at the top of the channel be equal to  $-0.5$ . Note that in our model the reflection coefficients, for simplicity, account for both absorption at channel ends and attenuation along the channel. So, they should be viewed as effective reflection coefficients.

[17] Figure 4a shows currents computed using equations (A1) and (A2) (see Appendix A) at the bottom ( $z = h_1$ ), middle ( $z = h_1 + \Delta h/2$ ), and top ( $z = h_2$ ) of the 100 m long channel; peak currents at these heights are 40, 34, and 32 kA, respectively. They are not much different from each other (currents at the channel ends are within less than 20% of the current in the middle). A three-dimensional

plot of current as a function of both time and height is shown in Figure 4b. Note that the incident current wave peak is 50 kA, while the equivalent current distribution along the channel peaks at 32 to 40 kA, due to reflections (absorption at the ends). Further, the overall current wave-shapes at these three positions along the channel are similar. Half-peak widths are 7.0  $\mu$ s, 8.2  $\mu$ s, and 8.6  $\mu$ s, although the waveforms in the middle and at the top are shifted by 0.25 and 0.5  $\mu$ s, respectively, relative to the waveform at the bottom. Figure 4c shows the total current (including reflections, if any) along the channel at  $t = 0.5, 4, 8,$  and 16  $\mu$ s after the incident current wave starts moving upward from the bottom of the channel. Note that at  $t = 8 \mu$ s (not far from the current peak) the distribution of total current along the channel is essentially uniform. The more or less uniform distribution of current along the CID channel is apparently due to relatively short channel length, relatively long current waveforms, and relatively high propagation speed.

[18] Our observation that the current distribution along the CID channel is not much different from uniform suggests that CID can be viewed as a Hertzian (electrically short) dipole. In part 2 [*Nag and Rakov*, 2010], we will show that some CIDs can be approximated by vertical Hertzian dipoles. This approximation will enable us to simplify the field equations and use measured fields to infer various electrical parameters of CIDs (within this approximation, the propagation speed and reflection coefficients are not input parameters and the current waveshape is the same as that of the time integral of NBP). In section 7, we compute CID electric field waveforms using the Hertzian dipole approximation and compare them with their counterparts computed in section 6 using the bouncing-wave model. In Appendix C, fields predicted by the Hertzian dipole approximation are compared with those measured by *Eack* [2004].

## 6. Bouncing-Wave Model: Electric Fields at 2 and 200 km

[19] The general time domain equation for computing the vertical electric field  $dE_z$  due to a vertical differential current element  $idz$  (vertical dipole of length  $dz$  carrying a uniform current  $i(t)$ ) at a height  $z$  above a perfectly conducting ground plane for the case of an observation point P on the plane at a horizontal distance  $r$  from the dipole is given by [e.g., *Uman*, 1987; *Thottappillil et al.*, 1997],

$$dE_z(r,t) = \frac{1}{2\pi\epsilon_0} \left[ \frac{(2z^2 - r^2)}{R^5(z)} dz \int_{t_b(z)}^t i\left(z, \tau - \frac{R(z)}{c}\right) d\tau + \frac{(2z^2 - r^2)}{cR^4(z)} i\left(z, t - \frac{R(z)}{c}\right) dz - \frac{r^2}{c^2 R^3(z)} \frac{di\left(z, t - \frac{R(z)}{c}\right)}{dt} dz \right], \quad (2)$$

where  $\epsilon_0$  is the electric permittivity of free space,  $c$  is the free-space speed of light,  $t_b(z)$  is the time at which the current is "seen" by an observer to begin at height  $z$ ,  $R$  is the inclined distance from the dipole to the observation point, which is given by  $R(z) = \sqrt{z^2 + r^2}$  (see Figure 5).

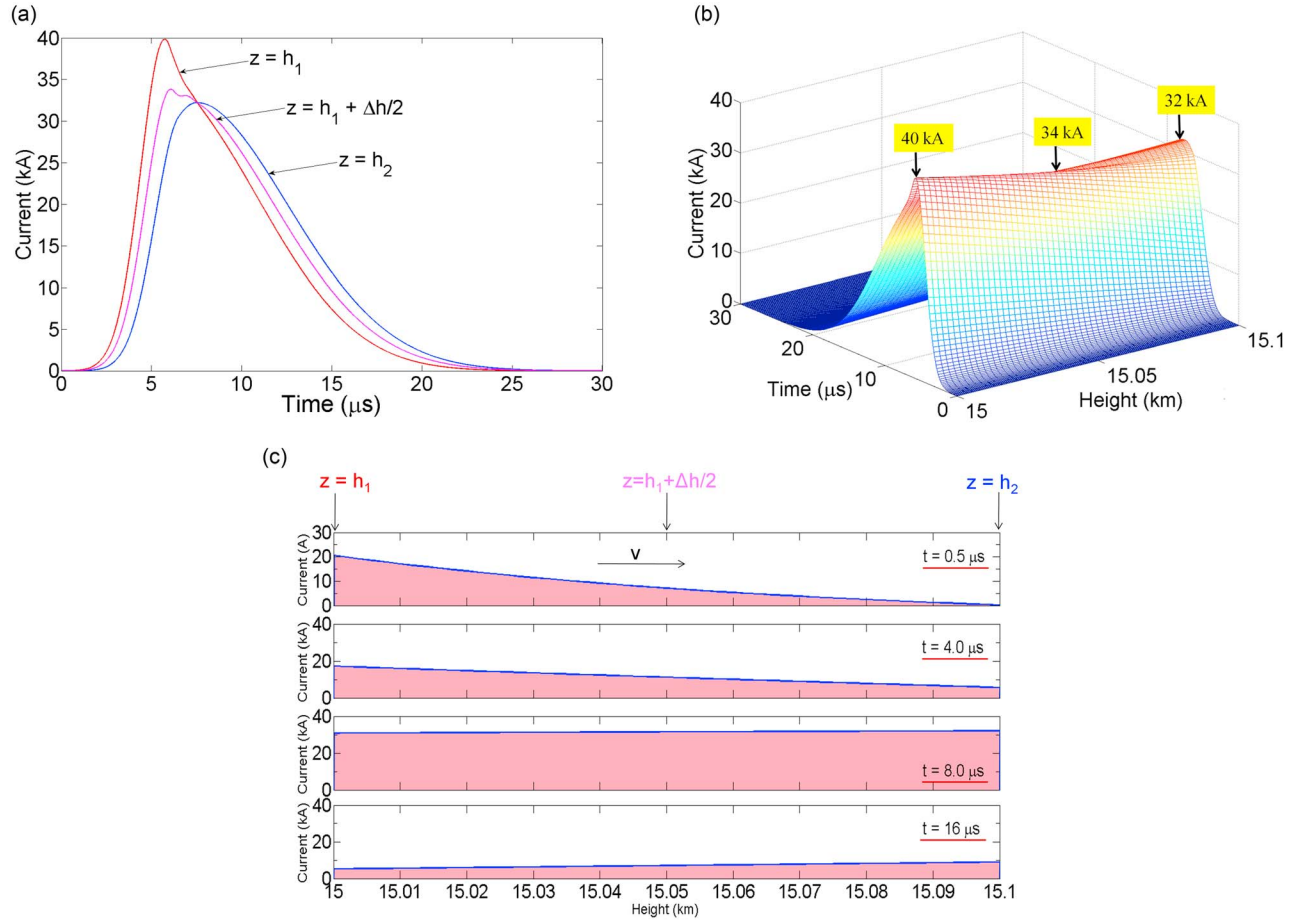


**Figure 4.** (a) Currents computed using equations (A1) and (A2) (see Appendix A), at the bottom ( $z = h_1$ ), middle ( $z = h_1 + \Delta h/2$ ), and top ( $z = h_2$ ) of the channel for a CID characterized by  $h_1 = 15$  km,  $\Delta h = 100$  m,  $v = 2 \times 10^8$  m/s,  $\rho_t = \rho_b = -0.5$ ,  $I_p = 50$  kA, and zero-to-peak current risetime  $RT = 6 \mu\text{s}$ ; peak currents at these three heights are 40, 34, and 32 kA, respectively. They are not much different from each other (currents at the channel ends are within less than 20% of the current in the middle). (b) A three-dimensional plot of current as a function of both time and height. Note that the incident current wave peak is 50 kA (as shown in Figure 3a), while the equivalent current distribution along the channel peaks at 32 to 40 kA, due to reflections (absorption at the ends). (c) The total current (including reflections, if any) along the channel at  $t = 0.5, 4, 8,$  and  $16 \mu\text{s}$  after the incident current wave starts moving upward from the bottom of the channel. Note that at  $t = 8 \mu\text{s}$  (not far from the current peak) the distribution of current along the channel is essentially uniform. Note that in Figure 4c the current scale of the first panel is different from that of the other three panels.

[20] From equation (2) for the geometry shown in Figure 5, the total electric field at the observation point for a finite-length channel whose lower and upper ends are at altitudes of  $h_1$  and  $h_2$ , respectively, is given by

$$\begin{aligned}
 E_z(r, t) = & \frac{1}{2\pi\epsilon_0} \int_{h_1}^{h_2} \left[ dz \frac{(2z^2 - r^2)}{R^5(z)} \int_{t_b(z)}^t i\left(z, \tau - \frac{R(z)}{c}\right) d\tau \right. \\
 & + \frac{(2z^2 - r^2)}{cR^4(z)} i\left(z, t - \frac{R(z)}{c}\right) dz \\
 & \left. - \frac{r^2}{c^2 R^3(z)} \frac{di\left(z, t - \frac{R(z)}{c}\right)}{dt} dz \right], \quad (3)
 \end{aligned}$$

where  $h_2$  is a function of time during the first traversal of the channel.

[21] Figure 6a shows the electrostatic, induction, and radiation field components, and total electric field predicted by the bouncing-wave model at a horizontal distance of 2 km. Current distribution shown in Figure 4 was used in the calculations. As expected, the static and induction components are dominant at 2 km (radiation nearly along the axis of a vertical dipole is negligible). Figure 6b shows the total electric field (essentially the same as its radiation component) at a horizontal distance of 200 km. At least two secondary peaks can be seen in the electric field waveform shown in Figure 6b. Figure 6c shows the electric field derivative at 200 km, in which one can discern four cycles of oscillations after the primary cycle. The time interval between consecutive maxima in the  $dE/dt$  signature is  $1 \mu\text{s}$  which corresponds to the round trip time of the current pulse along the channel, that is, from bottom to top and back. The

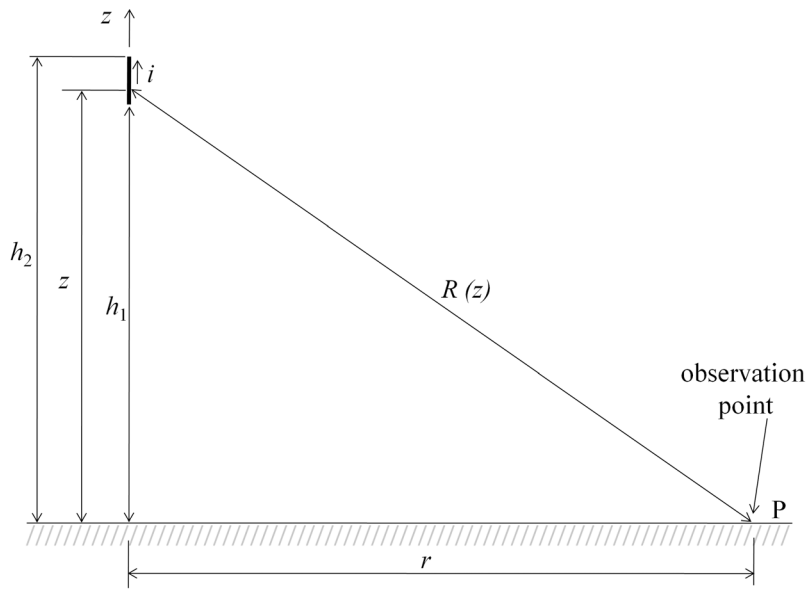


**Figure 5.** Geometrical parameters used in calculating the electric field at observation point P on perfectly conducting ground at horizontal distance  $r$  from the vertical CID channel extending between heights  $h_1$  and  $h_2$ . See text for details.

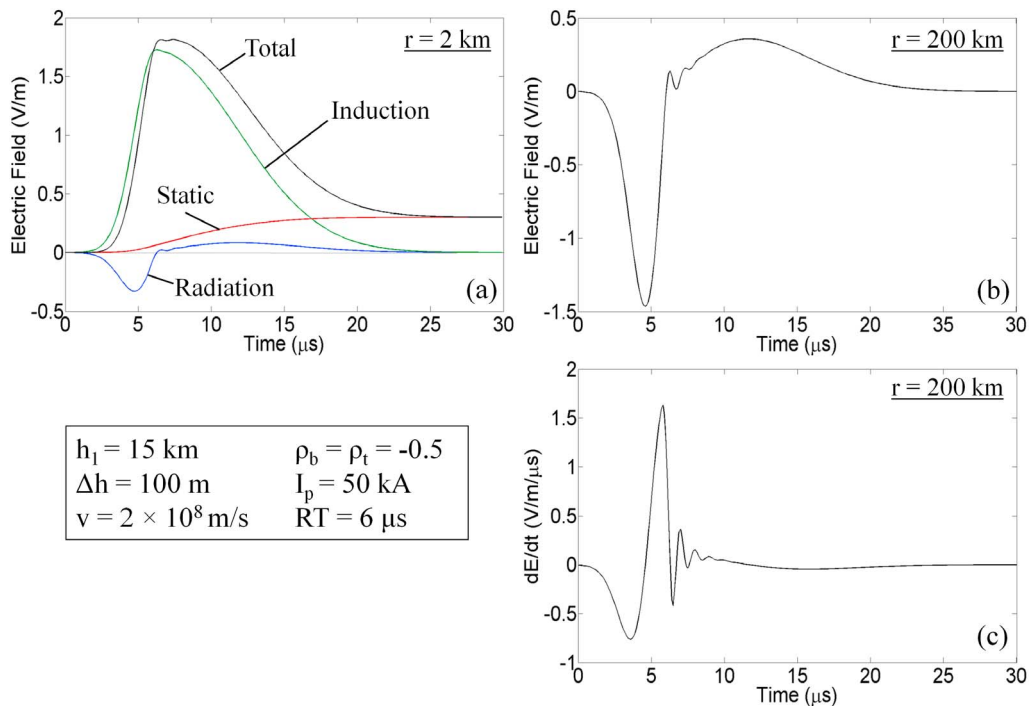


**Figure 6.** (a) Electrostatic, induction and radiation field components, and total electric field predicted by the bouncing-wave model at a horizontal distance of 2 km. As expected, the static and induction components are dominant at this distance. (b) Total electric field (essentially the same as its radiation component) at a horizontal distance of 200 km. At least two secondary peaks can be seen in the electric field waveform. (c) The electric field derivative at 200 km, in which one can discern four cycles of oscillations after the primary cycle. The time interval between consecutive maxima in the  $dE/dt$  signature is  $1 \text{ } \mu\text{s}$  which corresponds to the round trip time of the current pulse along the channel, that is, from bottom to top and back.

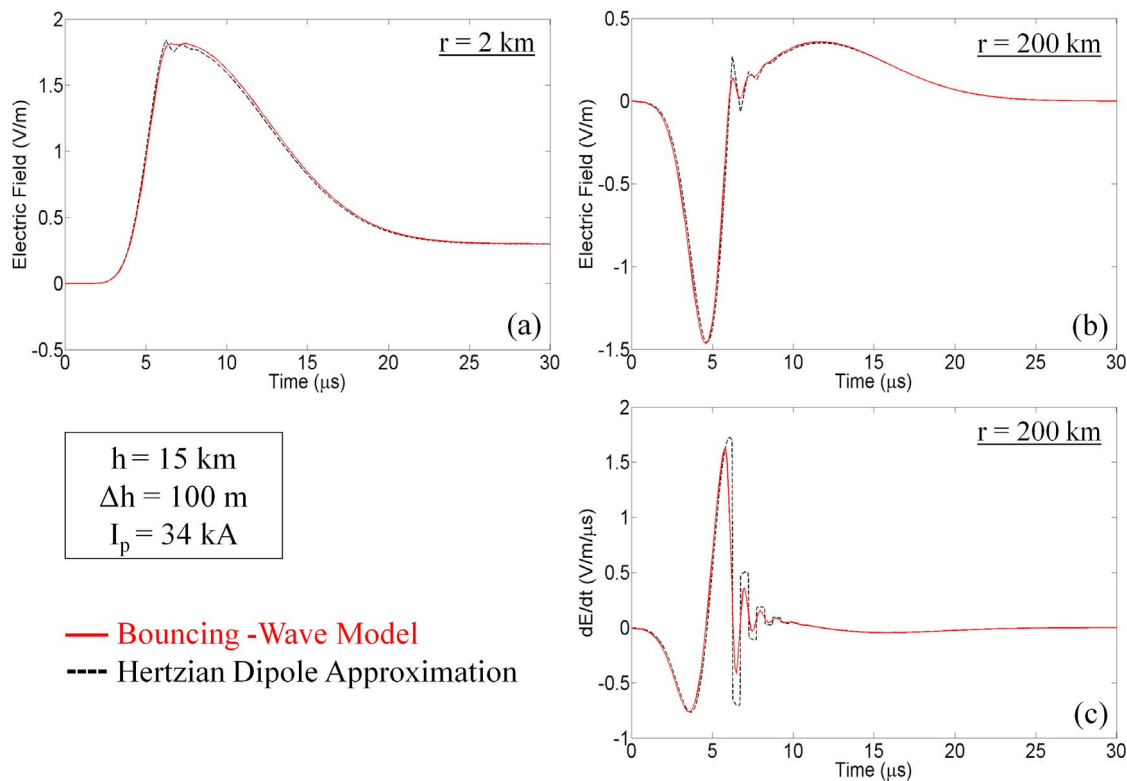


**Figure 7.** Electric fields at (a) 2 km and (b) 200 km computed using the Hertzian dipole approximation for a CID with a channel length of 100 m at a height of 15 km, excited by current waveform shown in Figure 4a for  $z = h_1 + \Delta h/2$  (in the middle of the channel). The current peak,  $I_p$ , is 34 kA. (c) The corresponding  $dE/dt$  signature at 200 km. Electric fields and  $dE/dt$  computed using the bouncing wave model and presented in Figure 6 are also shown here for direct comparison. A good match is evident in each of the three panels.

half period ( $0.5 \mu\text{s}$ ) is the travel time of the current pulse in one direction.

[22] In Appendix B, we used our bouncing-wave model to compute distant electric field waveforms and compare them with measurements. We varied model parameters, such as current wave propagation speed, channel length, current reflection coefficients, and current risetime, in order to examine effects of these variations on fields predicted by the bouncing-wave model. We found that that model-predicted fields are consistent with measurements only for relatively narrow ranges of these parameters. Specifically, we estimated that the effective current reflection coefficients (assumed to be the same) at channel ends should be approximately in the range of 0 to  $-0.5$ , the wave propagation speed ranges from about  $0.3$  to  $3 \times 10^8$  m/s, and the channel length is less than about 1000 m. The lower bound on channel length was assumed to be about 100 m, based on observed reflection signatures in  $dE/dt$  records. Influence of current risetime on field waveforms was also examined, and this parameter was found to be typically in the range from about 2 to  $8.5 \mu\text{s}$ . We also determined the “allowed” combinations of parameters.

[23] In Appendix C, we test the validity of the bouncing-wave model using electric fields simultaneously measured at near and far distances by *Eack* [2004]. A good match between model-predicted and measured fields is obtained

for a peak current of 75 kA, zero-to-peak current risetime of  $5.2 \mu\text{s}$ , propagation speed of  $1.4 \times 10^8$  m/s, channel length of 650 m, and current reflection coefficients at channel ends equal to zero.

## 7. Hertzian Dipole Approximation

[24] Equation (2) also applies to a vertical dipole of finite length  $\Delta h$  at height  $h$ , provided that  $\Delta h$  is very short compared to the shortest significant wavelength  $\lambda$  (Hertzian dipole approximation). For a vertical Hertzian dipole we can replace  $dz$  with  $\Delta h$  in (2) to get:

$$E_z(r, t) = \frac{1}{2\pi\epsilon_0} \left[ \frac{(2h^2 - r^2)\Delta h}{R^5} \int_{t_b}^t i(\tau - R/c) d\tau + \frac{(2h^2 - r^2)\Delta h}{cR^4} i(t - R/c) - \frac{r^2\Delta h}{c^2R^3} \frac{di(t - R/c)}{dt} \right]. \quad (4)$$

[25] Note that the current in equation (4), is the same everywhere along the dipole (independent of  $z$ ). In Figures 7a and 7b we compare electric field waveforms at  $r = 2$  km and  $r = 200$  km, respectively, computed using the Hertzian dipole approximation (equation (4)) with their

counterparts computed using the bouncing-wave model. The Hertzian dipole, assumed to be 100 m in length and located at a height of 15 km above ground, was excited by the current found for the middle of the channel ( $z = h_l + \Delta h/2$ ) using the bouncing wave model (see Figure 4a). Figure 7c shows the  $dE/dt$  waveforms at 200 km computed using the Hertzian dipole approximation and the bouncing wave model. Clearly, the fields computed using the Hertzian dipole approximation closely match those based on the bouncing-wave model. Note, however, that for longer channels, slower speeds, and shorter current risetimes, the Hertzian dipole approximation may not be applicable. Limits of validity of the Hertzian dipole approximation in terms of these parameters are discussed by *Nag and Rakov* [2010].

[26] In Appendix C, we test the validity of the Hertzian dipole approximation using electric fields simultaneously measured at near and far distances by *Eack* [2004]. A good match between model-predicted fields and the experimental data is obtained for a peak current of 74 kA, zero-to-peak current risetime of 9  $\mu\text{s}$ , and channel length of 500 m. The CID parameters providing a good match with the experimental data for the Hertzian dipole approximation are not much different (particularly the peak current) from those for the bouncing-wave model (see section 6).

## 8. Discussion

[27] *Smith et al.* [1999] estimated the CID channel lengths to range from 300 to 1000 m. In estimating the lower bound, they considered two oppositely charged spherical regions, immediately adjacent to each other, with the CID channel extending between the centers of the two spheres (see section 5 of part 2 [*Nag and Rakov*, 2010] for more details). The lower bound on channel length was found by comparing the maximum electric field (at the point of contact of the spheres), for the average CID charge transfer estimated from observations, with the conventional breakdown electric field in the cloud (on the order  $10^6$  V/m). The upper bound on channel length of 1000 m was apparently based on the median measured duration of 3.2  $\mu\text{s}$  of HF radiation produced by CIDs [*Smith*, 1998] and the upper limit for the propagation speed of  $3 \times 10^8$  m/s. Our channel lengths estimated from channel traversal times measured in  $dE/dt$  records are smaller than *Smith et al.*'s lower bound of 300 m, with the corresponding charge configuration being discussed in part 2 [*Nag and Rakov*, 2010]. The upper bound on CID channel length estimated in this study (see Appendix B) by comparing bouncing-wave model predicted electric fields to measurements is the same as that of *Smith et al.* [1999].

[28] Using the upper bound on channel length and the mean duration (10–90%) of 13.7  $\mu\text{s}$  of CID dipole moment change, *Smith et al.* [1999] calculated the propagation speed of the current wave to be  $7.3 \times 10^7$  m/s. According to the bouncing-wave mechanism proposed in this paper, the average propagation speed inferred by *Smith et al.* [1999], who essentially assumed that the total duration of the CID electric field pulse is equal to one channel traversal time, must be an underestimate, although it is within the range of allowed values (see Appendix B).

[29] *Eack* [2004] erroneously used the dipole approximation to infer the propagation speed for CIDs from his

two-station electric field measurements. In doing so, he estimated the dipole moment change,  $\Delta p$ , from a close field record, which at later times is dominated by the electrostatic field component. From the electrostatic field change,  $\Delta E_{es}$ , measured at distance  $r$ , the dipole moment change is

$$\Delta p = 4\pi\epsilon_0\Delta E_{es}r^3. \quad (5)$$

This step is fine, but then *Eack* substituted the resultant  $\Delta p$  value into the equation for dipole moment change in terms of the radiation electric field change,  $\Delta E_r$ , at distance  $r$  (much larger than  $r$  in equation (5)),

$$\Delta p = 4\pi\epsilon_0c^2r \int \int \Delta E_r(t)dt, \quad (6)$$

where  $c$  is the speed of light (speed at which an electromagnetic wave propagates from the source to the observer), which he labeled as “ $v$ ” and misinterpreted as the propagation speed of the CID current wave along the channel. The propagation speed along the channel is not a parameter of the dipole approximation and, hence, it cannot be derived from this approximation. In fact, solving equation (6) for  $c$  should yield  $3 \times 10^8$  m/s, and any deviation from this value (*Eack* computed  $1.5 \times 10^8$  m/s, on average) should be viewed as being due to inadequacy of employed model and/or measurement errors. Further, *Eack* used his misinterpreted propagation speed and the total duration of the CID electric field pulse to estimate the CID channel length. The resultant (incorrect) average channel length for seven CIDs was 3.2 km (larger than the upper bound estimated in Appendix B).

[30] *Hamlin et al.* [2007] inferred that the secondary peak (of the same polarity as the preceding primary peak) in CID electric field signatures was due to reflection of the current wave from the far end of the channel. They used an assumed propagation speed of  $3 \times 10^8$  m/s and the time difference between the primary and secondary peaks to estimate the upper bound on channel length, which was found to be 2 km. However, as we found from modeling (see section 6), the secondary peaks observed by *Hamlin et al.* [2007] actually occur at the time when the current front is in the middle of the channel, after being reflected from its far end. More importantly, the secondary peak, occurring several microseconds after the primary peak, results from one of the higher-order reflections from the far end of the channel, as evident from comparison of simultaneously measured electric field and  $dE/dt$  signatures in Figure 1. It follows that *Hamlin et al.*'s channel lengths are overestimates. In Appendix B, we estimated the upper bound on CID channel length to be about 1000 m. Longer channels would result in distant electric field waveforms that are inconsistent with experimental data.

[31] *Watson and Marshall* [2007] used the original transmission line (TL) model [*Uman et al.*, 1975] and a modified TL model with an exponentially increasing current along the channel to compute electric field signatures at horizontal distances of 2.8 and 200 km and compare them with corresponding measured waveforms reported by *Eack* [2004]. Both models can, in principle, successfully match the two-station field measurements (for the TL model after a slight change in distance from the close station). The exponentially increasing current was assumed by *Watson*

and Marshall to correspond to the runaway electron breakdown process. They estimated the propagation speed and channel length to be  $6 \times 10^7$  m/s and 630 m, respectively, for the exponentially increasing current model. For the TL model (constant amplitude of current wave) they estimated a speed of  $2 \times 10^8$  m/s and a channel length of 500 m. Watson and Marshall's estimates of propagation speed and channel length are within the range of allowed values found in Appendix B.

[32] In this study, we assume that the shortest CID channel length is about 100 m and show, via comparison of bouncing-wave model predictions with measurements, that the upper bound on channel length is approximately 1000 m. Thus, compact intracloud discharges are indeed "compact." The uniqueness of CIDs is apparently related to the fact that a short conducting channel (its length is primarily determined by the spatial extent of high-field region) is created faster (on a submicrosecond time scale) than the cloud electric field can polarize this channel (make it nearly equipotential). This mismatch results in a transient, bouncing-wave process in the channel. The polarization rate should be primarily determined by the conductivity of the channel, which for a "lightning seed" created via a runaway electron breakdown process is expected to be on the order of  $10^{-4}$  S/m [Solomon *et al.*, 2001]. It is possible that the bouncing waves serve to maintain channel conductivity. As evidenced by a more or less constant period of oscillations (see Figure 1b), the channel length remains constant in the later part of the discharge. This short and fixed channel length property (although there should be corona-like streamers developing from channel ends) implies that CIDs cannot pervade large cloud volumes and tap remote charge reservoirs, which is consistent with the fact that the majority CIDs tend to occur in isolation from any other lightning activity. On the other hand, CIDs apparently can and do cause charge redistribution in the cloud, which may facilitate or contribute to initiation of "normal" IC discharges or influence development of CG discharges [e.g., Rison *et al.*, 1999; Thomas *et al.*, 2001; Krehbiel *et al.*, 2008; Nag *et al.*, 2010].

## 9. Summary

[33] We examined the electric field derivative (dE/dt) signatures of 212 CIDs in Florida and found multiple secondary peaks (oscillations), which are indicative of reflections, in 15% of them. It is likely that the waveforms showing pronounced reflections correspond to shortest CID channels. The shortest radiating channel length appears to be about 100 m. On the basis of the experimental evidence of multiple reflections and modeling, we infer that, from the electromagnetic point of view, the CID is essentially a bouncing-wave phenomenon. Some tens of reflections may occur at both radiating-channel ends. The process can be viewed as a long wave repeatedly folding on itself, so that the electromagnetic signature duration is not necessarily a measure of radiator length. It is possible that the bouncing waves serve to maintain channel conductivity. Only higher-order reflections (in the later portion of the waveform) are detectable (if at all) in either electric field or dE/dt waveforms, while the undetectable lower-order reflections do influence the magnitude of the primary CID signature. In about 85% dE/dt signatures no reflections were observed.

Factors that can make reflections undetectable include a relatively small magnitude of the incident wave, relatively long radiating channel, relatively large losses along the channel, and a relatively small (in absolute value) current reflection coefficients at channel ends. Reflections at channel extremities may result in corona-like electrical breakdown there, because a reduction of current is accompanied by an increase of line charge density and associated voltage (voltage doubles at an open circuit end and increases by a factor of 1.5 if the current reflection coefficient is equal to  $-0.5$ ). This breakdown at channel ends is likely to produce intense bursts of HF-VHF radiation and increase "noisiness" of dE/dt signatures, which are both characteristic features of CIDs. Thus, reflections may be responsible for the fine structure of wideband electric field and dE/dt waveforms and, by inference, for "noisiness" of dE/dt waveforms and for accompanying HF-VHF radiation bursts.

[34] We modeled the CID as a wave traveling on an elevated vertical transmission line. In order to account for multiple reflections that take place at the channel ends we specified two equivalent current sources, connected at the bottom and at the top of the channel. By comparing model-predicted electric fields with measurements we estimated that effective current reflection coefficients at channel ends should be in the range of 0 to  $-0.5$ , that the wave propagation speed ranges from 0.3 to  $3 \times 10^8$  m/s, and that the channel length is less than 1000 m. In these calculations, we assumed that the current wave had a zero-to-peak risetime of  $6 \mu\text{s}$  and a total duration of  $30 \mu\text{s}$ . Influence of current risetime on field waveforms was also examined, and it was found to be typically in the range from about 2 to  $8.5 \mu\text{s}$ . The bouncing-wave model is capable of reproducing the entire spectrum of observed wideband electromagnetic signatures of CIDs (both with and without evidence of reflections).

[35] The current distribution along the CID channel is often not much different from uniform, as expected for a Hertzian (electrically short) dipole, because of relatively short channel length, relatively long current waveform, and relatively high propagation speed. Both the bouncing-wave model and the Hertzian dipole approximations are capable of reproducing two-station CID electric field measurements of Eack [2004]. Electrical parameters of CIDs are considered in part 2 [Nag and Rakov, 2010].

## Appendix A: Equivalent Current Sources to Represent Multiple Traveling Waves in the Bouncing-Wave Model

[36] An elevated vertical CID channel is modeled as a transmission line with impedance mismatch at either end. As a result, reflections are produced when the traveling current pulse hits channel ends. We assume that the line is uniform and that any losses along the line are accounted for in the reflection coefficients at the ends. So, the reflection coefficients used here are effective reflection coefficients. Although there will likely be a corona-like discharge (a nonlinear process) at either end of the line, we assume the effective reflection coefficients to be constant. The distribution of current along the channel can be expressed in terms of the incident current,  $i_0(t)$ , channel length,  $\Delta h$ , current wave speed,  $v$ , and effective current reflection coefficients at the top,  $\rho_t$ , and the bottom,  $\rho_b$ , of the channel. In the model considered here

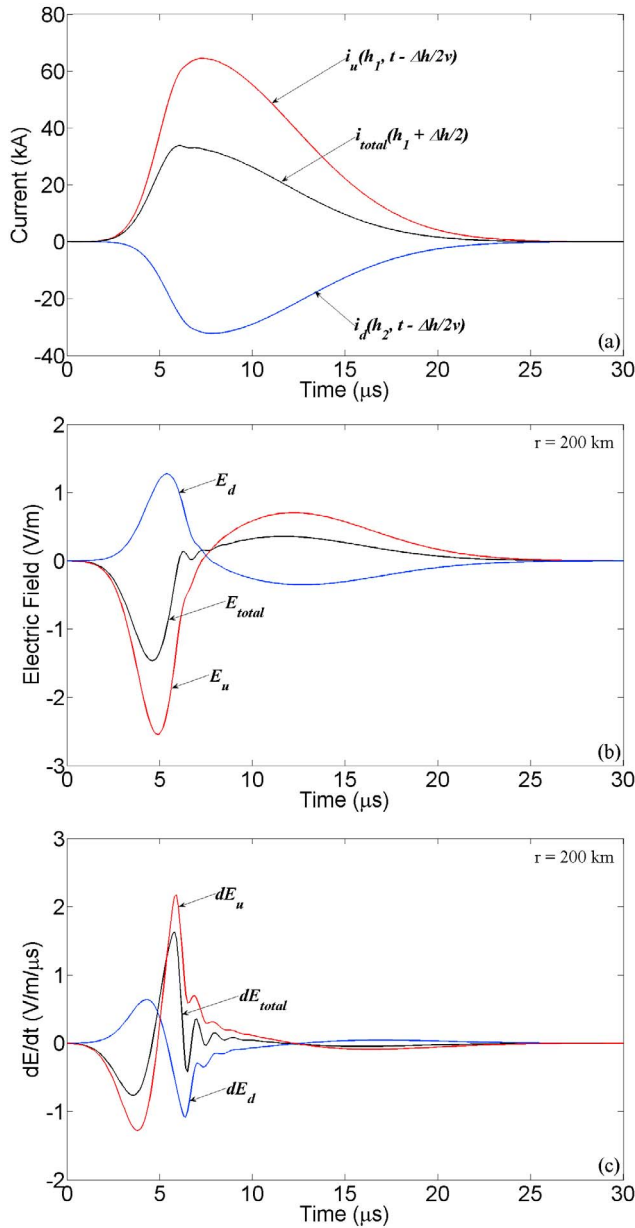


**Figure A1.** (a) The total current ( $i_{total}$ ) and its upward ( $i_u$ ) and downward ( $i_d$ ) components in the middle of the channel, (b) the total electric field and its components at 200 km corresponding to currents shown in Figure A1a, and (c) corresponding electric field derivatives.

we assume that the channel is already created and an incident current  $i_0(t)$  is injected at the bottom of the channel. Then the sum of upward traveling current waves (incident wave and all reflections from the channel bottom) is given by

$$i_u(h_1, t) = i_0(h_1, t) + \rho_i \rho_b i_0\left(h_1, t - \frac{2\Delta h}{\nu}\right) + \rho_i^2 \rho_b^2 i_0\left(h_1, t - \frac{4\Delta h}{\nu}\right) + \dots = \sum_{n=1,3,5,\dots}^{\infty} \rho_i^{n-1} \rho_b^{n-1} i_0\left(h_1, t - \frac{(n-1)\Delta h}{\nu}\right). \quad (A1)$$

Similarly, for the sum of downward traveling current waves (all reflections from the channel top) we have

$$i_d(h_2, t) = \sum_{n=2,4,6,\dots}^{\infty} \rho_i^{\frac{n}{2}-1} \rho_b^{\frac{n}{2}-1} i_0\left(h_2, t - \frac{(n-1)\Delta h}{\nu}\right). \quad (A2)$$

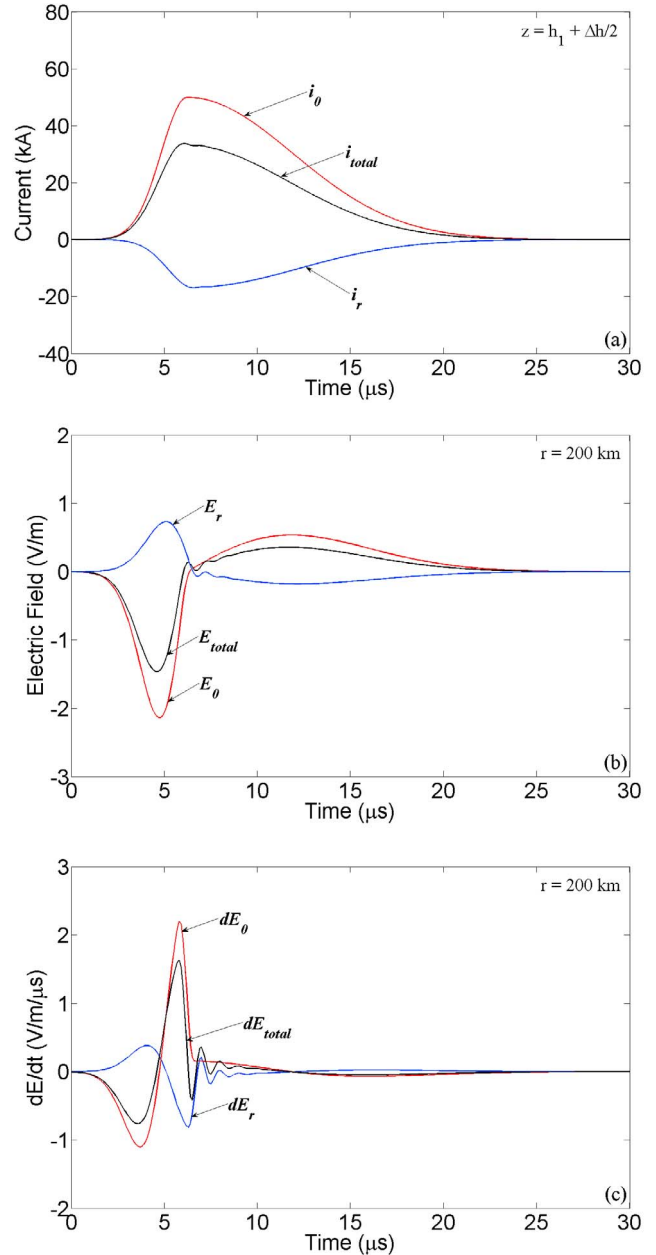


**Figure A2.** (a) The incident current ( $i_0$ ), the sum of all reflections ( $i_r$ ), and the total current ( $i_{total}$ ) in the middle of the channel, (b) the electric field components and the total field at 200 km corresponding to currents shown in Figure A2a, and (c) corresponding electric field derivatives. Note that while the incident current moves upward along the channel, the sum of all the reflections contains both upward and downward moving components.

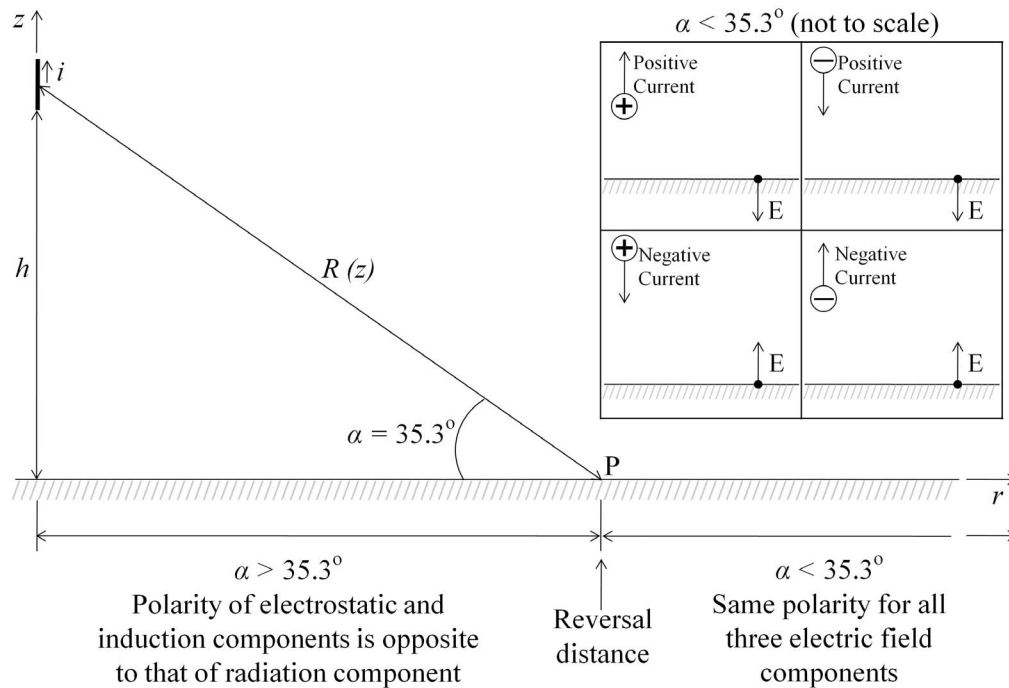


**Figure A3.** Illustration of the reversal distance for electrostatic and induction electric field components. Inset shows the direction of the far ( $\alpha < 35.3^\circ$ ) electric field vector for different combinations of charge polarity and direction of charge motion. In case of bipolar electric field signature (dominated by its radiation component) the direction of electric field vector refers to the initial half cycle.

These two expressions specify equivalent current sources connected at the channel ends. The two sources launch current waves toward each other and the total current at any position  $z$  along the channel can be obtained by appropriately shifting and combining  $i_u(h_1, t)$  and  $i_d(h_2, t)$ . For example, at  $z = h_1 + \frac{\Delta h}{2} = h_2 - \frac{\Delta h}{2}$ ,  $i(h_1 + \frac{\Delta h}{2}) = i_u(h_1, t - \frac{\Delta h}{2v}) + i_d(h_2, t - \frac{\Delta h}{2v})$ . The total current and its two components in the middle of the channel are shown in Figure A1a. Additionally, in Figure A2a we show the incident current ( $i_0$ ), the sum of all reflections ( $i_r$ ), and the total current ( $i_{total}$ ) in the middle of the channel. Note that while the incident current moves upward along the channel, the sum of all the reflections contains both upward and downward moving components. Electric field components and total fields at 200 km corresponding to currents shown in Figures A1a and A2a are presented in Figures A1b and A2b and field derivatives in Figures A1c and A2c, respectively. For computing the currents and fields shown in Figures A1 and A2, we used  $\Delta h = 100$  m,  $v = 2 \times 10^8$  m/s, and  $\rho = -0.5$ .

[37] We now discuss sign conventions used in this study. As noted by Nag *et al.* [2010], for a short vertical dipole at relatively large elevation angle  $\alpha$  above ground (see Figure A3) the radiation electric field peak on the one hand and induction and static field changes on the other are expected to have opposite polarities. Specifically, it follows from equation A.38 of Uman [1987, p. 329] for the electric field at perfectly conducting ground due to a differential vertical dipole that the opposite polarities are expected

for  $\alpha > 35.3^\circ$ , which translates to  $r < 21$  km if source height  $h = 15$  km. The horizontal distance  $r$  at which the static and induction components change direction is equivalent to the well-known [e.g., Rakov and Uman, 2003, chapter 3] reversal distance for the electrostatic field due to an elevated finite-length vertical dipole.

[38] We assume that a positive charge moving in the positive  $z$  direction (vertically upward) constitutes a positive current. Due to the first reflection from the top of the channel, the current is flipped in polarity (current reflection coefficient is negative). As a result of the next reflection, from the bottom of the channel, the polarity will be flipped again. Hence,  $i_u$ , the sum of upward-traveling current waves (incident wave and all reflections from the bottom), is positive, while  $i_d$ , the sum of downward-traveling current waves (all reflections from the top), is negative.

[39] At far distances ( $\alpha < 35.3^\circ$ ), the electric field change is essentially equal to its radiation component. Motion of positive charge upward (or negative charge moving downward) produces a radiation electric field change (initial peak) directed downward as shown in Figure A3 (inset). Conversely, for motion of positive charge downward (or negative charge moving upward) the radiation electric field is directed upward. At close distances (for  $\alpha > 35.3^\circ$ ), motion of positive charge upward (or negative charge moving downward) produces electrostatic and induction field changes directed upward and radiation electric field change directed downward.

[40] According to the physics sign convention [e.g., Rakov and Uman, 2003; chapter 1], a downward directed

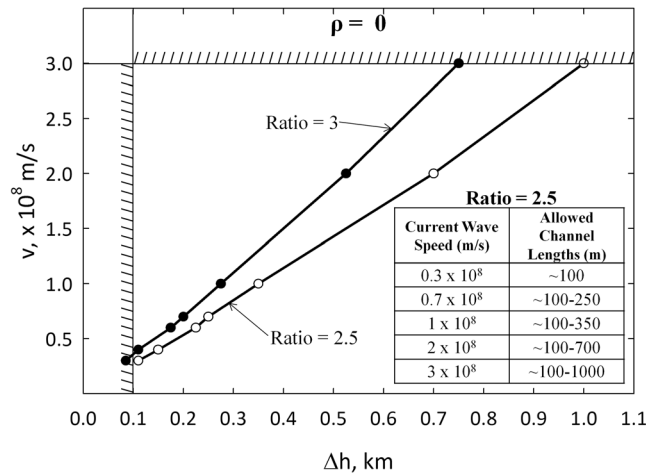


**Figure B1a.** Combinations of propagation speed and channel length for which the ratio of initial electric field peak to opposite polarity overshoot of model-predicted electric fields at 200 km attains 2.5 (the lowest value found in the experimental data) and 3.0 for a current risetime of 6 μs and ρ = 0. The area limited by the v = 3 × 10<sup>8</sup> m/s, Δh = 0.1 km, and ratio = 2.5 lines defines the domain of “allowed” combinations of v and Δh.

electric field vector is assumed to be negative. We use the physics sign convention throughout this paper.

**Appendix B: Bouncing-Wave Model—Allowed Ranges of Variation of Input Parameters**

[41] We have used our bouncing-wave model to compute distant electric field waveforms and compare them with measurements. The model input parameters, current wave propagation speed, channel length, effective current reflection coefficients, source height, and current risetime were allowed to vary. We found that model-predicted fields are consistent with experimental data only for relatively narrow ranges of these parameters.

**B1. Reflection Coefficients**

[42] The current reflection coefficient at either channel end is expected to be between -1 and 0. Positive reflection coefficients imply that the equivalent impedance of surrounding medium (or source region) is lower than the characteristic impedance of current-carrying channel, which is physically unreasonable. As the magnitude of the reflection coefficient increases the amplitudes of the secondary peaks in the electric field waveform become larger. As a result, the number of secondary peaks discernible in the electric field waveform increases with increasing the reflection coefficient magnitude. If we limit the number of secondary peaks detectable in the electric field waveform to three, then effective current reflection coefficients should be in the range from -0.5 to 0. Note that in our data set, 85% of the electric field waveforms do not exhibit any secondary peaks and in the remaining 15% typically only one secondary peak is observed. It is likely that actual current reflection coefficients are close to -1, while the effective values are lower in absolute value due to our lumping of

losses along the channel at the channel ends and combining those losses with absorption there. It is important to note that reflections do influence the overall field waveform, even when they are not detectable. All the field calculations presented in this appendix were performed for two values of ρ (assumed to be the same at both channel ends), 0 and -0.5.

**B2. Propagation Speed (v) and Channel Length (Δh)**

[43] The ratio of initial electric field peak to opposite polarity overshoot for distant CID electric field waveforms ranges from 2.5 to 14 in studies of Willett et al. [1989, Table 1] and Smith et al. [1999, Table 2]. In our data the ratio varies from 3.5 to 17 [Nag et al., 2010]. Either decreasing the current wave speed or increasing the channel length serves to decrease this ratio. Hence the smallest observed ratio (2.5) can be used to establish a lower bound for propagation speed and an upper bound for channel length; that is, “allowed” combinations of these two parameters. We additionally found “allowed” combinations of speed and channel length for the ratio equal to 3.

[44] The upper bound for speed is the speed of light, and the lower bound for channel length was set to be about 100 m. Nag and Rakov [2010] (part 2) showed that for 9 located CIDs for which we were able to estimate (assuming a speed of 2.5 × 10<sup>8</sup> m/s) channel lengths using oscillations in their measured dE/dt signatures, CID channel lengths range from 108 to 142 m. For a longer channel (all other conditions being the same), the current wave will generally be more attenuated while traversing it, and hence the reflected wave will be less pronounced. Thus it is logical to assume that the 9 events with most pronounced reflections are associated with the shortest channels. Note that, for all 32 CIDs (discussed in section 3), whose dE/dt signatures showed multiple secondary peaks (oscillations), including the 9 located ones, CID channel lengths range from 84 to 181 m, for an assumed speed of 2 × 10<sup>8</sup> m/s. The latter speed was considered to be the lower bound for the events with measured channel traversal times, since for lower speeds the channel length would become unreasonably small.

[45] We first present field calculations that were performed using the incident current wave shown in Figure 3a. Its zero-to-peak risetime is 6 μs and its total duration is 30 μs.

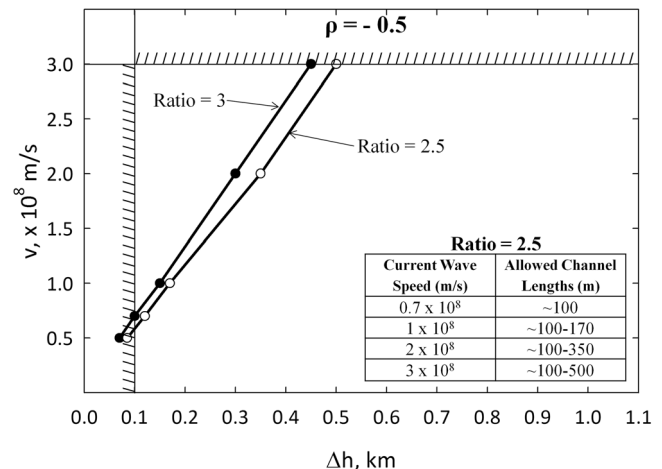


**Figure B1b.** Same as Figure B1a but for ρ = -0.5.

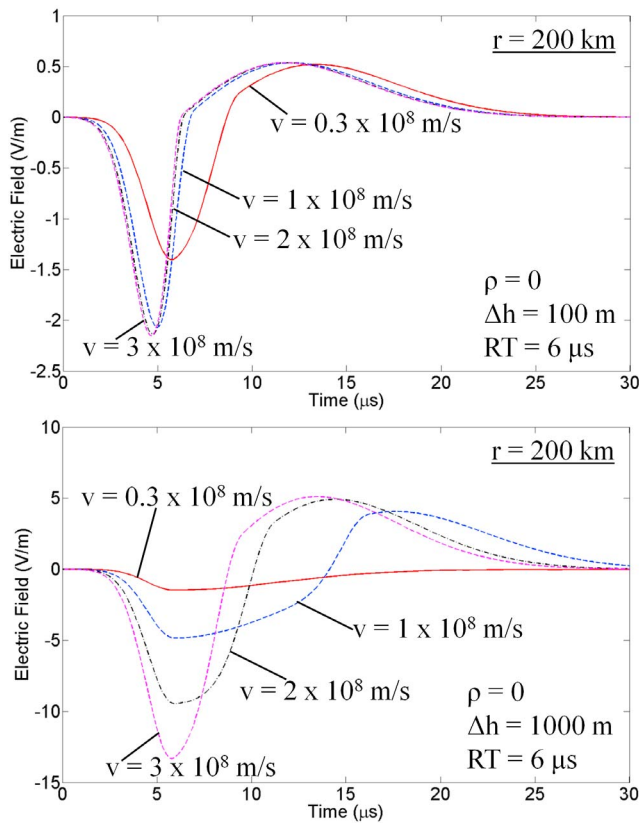


**Figure B2a.** Bouncing-wave model predicted electric fields at 200 km for different combinations of propagation speed and channel length for a current risetime of  $6 \mu\text{s}$  (the source current is described in section 5 and shown in Figure 3a) and  $\rho = 0$ .

Influence of current risetime will be examined later in this appendix. Figures B1a and B1b, show for  $\rho = 0$  and  $\rho = -0.5$ , respectively, different combinations of propagation speed and channel length for which the ratio of initial electric field peak to opposite polarity overshoot of model-predicted electric fields at 200 km attains 2.5 (the lowest value found in the experimental data) and 3.0 (included for comparison). It can be seen from Figure B1a that the largest allowed (within our model) value of channel length  $\Delta h$  for  $\rho = 0$  is about 1000 m. A larger  $\Delta h$  would result in a speed greater than  $3 \times 10^8 \text{ m/s}$ , which is not allowed. For the ratio equal to 3, the largest allowed  $\Delta h = 750 \text{ m}$ . For  $\rho = -0.5$ , one can see from Figure B1b that the upper bound for channel length is about 500 m (not much different for ratios of 2.5 and 3). Also, it can be seen from Figures B1a and B1b that for the lowest assumed value of channel length (100 m), the lowest allowed values of propagation speed are about  $0.3 \times 10^8 \text{ m/s}$  and  $0.7 \times 10^8 \text{ m/s}$  for  $\rho = 0$  and  $\rho = -0.5$ , respectively.

[46] Allowed channel lengths for different values of propagation speed and ratio = 2.5 are tabulated in Figures B1a and B1b. The overall upper bounds on  $\Delta h$  for  $\rho = 0$  and for  $\rho = -0.5$  are 1000 and 500 m, respectively. Note that  $\Delta h/v$  (channel traversal time), which yields the ratio equal to 2.5, is almost constant and equal to about  $3.6 \mu\text{s}$  and  $1.7 \mu\text{s}$  for  $\rho = 0$  and  $\rho = -0.5$ , respectively. These longest

allowed traversal times are about 0.6 and 0.3 times the current zero-to-peak risetime of  $6 \mu\text{s}$ .

[47] Transformations of distant electric field waveforms in response to variations in  $\Delta h$  and  $v$  are illustrated in Figure B2 for a current risetime of  $6 \mu\text{s}$ . Figures B2a and B2b show, for  $\rho = 0$  and  $\rho = -0.5$ , respectively, the model-predicted electric fields (the source current is described in section 5 and shown in Figure 3a) for four different propagation speeds and for two values of  $\Delta h$ . The latter are the assumed absolute lower bound (100 m) and the upper bound for each of the values of  $\rho$  (see Figure B1). For both values of reflection coefficient and for  $\Delta h = 100 \text{ m}$ , one can see that electric field waveforms for all four propagation speeds appear to be consistent with experimental data (ratio  $\geq 2.5$ ). However, the electric field waveforms for the upper bounds of channel lengths ( $\Delta h = 500 \text{ m}$  for  $\rho = -0.5$  and  $\Delta h = 1000 \text{ m}$  for  $\rho = 0$ ) are inconsistent with experimental data (the ratio  $\geq 2.5$  condition is not satisfied), except for the upper bound on the propagation speed ( $3 \times 10^8 \text{ m/s}$ ).

[48] We now consider the influence of source height and horizontal distance on the upper bounds on CID channel length estimated above.

[49] *Smith et al.* [2004] and *Nag et al.* [2010] reported the median CID source heights to be 13 km and 15 km, respectively. The range of variation in our data set is from 8.8 to 29 km. In the above calculations we assumed a typical source height of 15 km. The ratio of the initial peak to the opposite polarity overshoot of the model-predicted waveforms of CIDs at a particular distance changes with height. However, the changes are relatively small and the upper

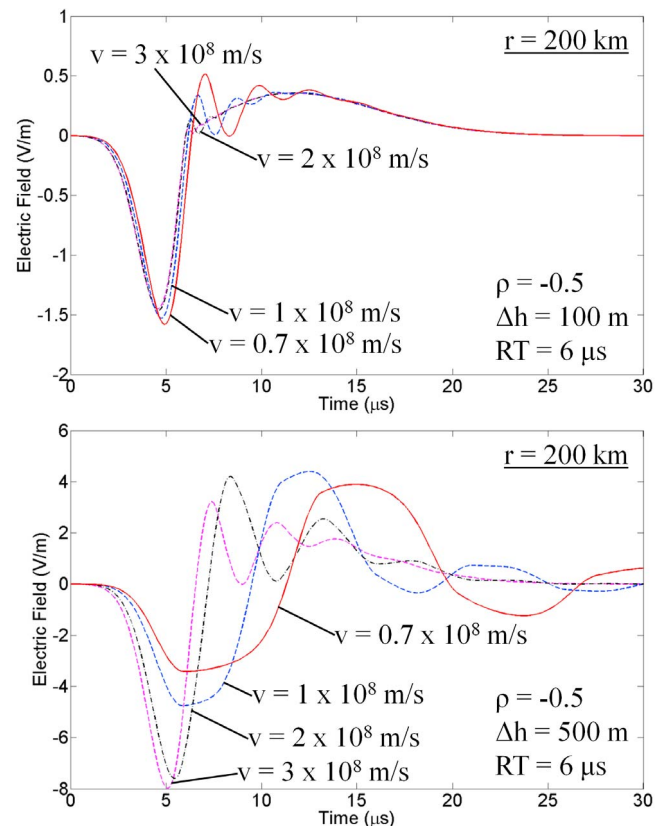


**Figure B2b.** Same as Figure B2a but for  $\rho = -0.5$ .

**Table B1.** Parameters  $g$  and  $k$  in Equation (B1) Yielding Different Values of Current Risetime ( $t_1$ )<sup>a</sup>

Current Risetime ( $\mu\text{s}$ )	$g$	$k = (t_2 - t_1)/t_1$
2	$50/t_2$	14
3	$32/t_2$	9
6	$15/t_2$	4
8.5	$10/t_2$	2.53
9	$10/t_2$	2.33

<sup>a</sup>The total duration of current pulse  $t_2$  remains the same and equal to  $30 \mu\text{s}$ .

bounds on channel length at different speeds remain essentially the same for different heights. For example, all other parameters remaining constant, the upper bounds on channel length at a distance of 200 km, for  $\rho = 0$  and  $v = 3 \times 10^8 \text{ m/s}$  are about 1100 m for a height of 5 km and about 1000 m for both 15 and 25 km.

[50] The ratio of the initial peak to the opposite polarity overshoot of the model-predicted waveforms of CIDs at a particular height changes with distance. This, in turn, would change the upper bound on channel length at different speeds. However, these changes are relatively small. For example, all other parameters remaining constant, the upper bounds on channel length for a source height of 15 km,  $\rho = 0$  and  $v = 3 \times 10^8 \text{ m/s}$  are 900, 1000, and 1100 m for distances of 50, 200, and 400 km, respectively. Similarly, for  $\rho = -0.5$  and  $v = 3 \times 10^8 \text{ m/s}$ , the upper bounds on channel length are about 600 m for 50 km and about 500 m for both 200 and 400 km.

### B3. Current Waveshape

[51] The expression for the current injected at the bottom end of the CID channel used in all our computations is an asymmetric Gaussian pulse with total duration  $t_2$  and zero-to-peak risetime of  $t_1$ . The expression for  $i_0(t)$  is given by

$$i_0(t) = \begin{cases} A e^{-(g(t-t_1))^2} & t \leq t_1 \\ A e^{-(g(t-t_1)/k)^2} & t > t_1 \end{cases} \quad (\text{B1})$$

where  $k = (t_2 - t_1)/t_1$ , and  $g$  is a parameter that, along with  $k$ , controls the shape of the pulse and causes current to approach zero at  $t = 0$  and  $t = t_2$ . In computing electric fields we have used a current pulse with a peak (A) of 50 kA and total duration ( $t_2$ ) of  $30 \mu\text{s}$ . In the following, we will examine the influence of zero-to-peak current risetime ( $t_1$ ), assuming that the total duration ( $t_2$ ) of current pulse remains the same at  $30 \mu\text{s}$ . The values of parameters  $g$  and  $k$  yielding different values of  $t_1$  are given in Table B1.

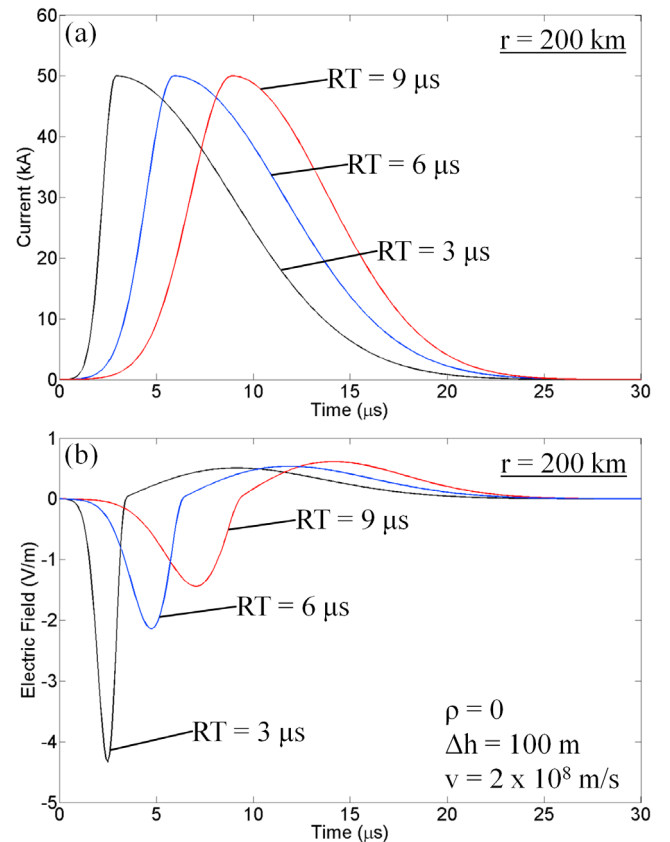
[52] In our model, for shorter channel lengths and higher speeds, the total width of the initial half cycle of the CID electric field signature tends to become equal to the risetime of the incident current pulse. This is clearly seen in Figure B2a where all field waveforms were computed for the same current risetime of  $6 \mu\text{s}$ . Electric field signatures produced by currents having the same total duration ( $30 \mu\text{s}$ ) and peak (50 kA), but different risetimes, 3, 6 and  $9 \mu\text{s}$ , are shown in Figure B3, for  $\rho = 0$ ,  $\Delta h = 100 \text{ m}$ , and  $v = 2 \times 10^8 \text{ m/s}$ ; the total duration of the initial half cycles of the electric field signatures are 3.4, 6.4, and  $9.3 \mu\text{s}$ , respectively. In our experimental data, the total duration of the initial half cycle

**Table B2.** Combinations of Reflection Coefficients, Propagation Speeds, and Channel Lengths That Produce Distant CID Electric Fields That are Consistent With Experimental Data for Current Risetime of  $3 \mu\text{s}$ 

Reflection Coefficient	Current Wave Speed (m/s)	Channel Length (m)
$\rho = -0.5$	$1.1 \times 10^8$	$\sim 100$
	$2 \times 10^8$	$\sim 100-175$
	$3 \times 10^8$	$\sim 100-275$
$\rho = 0$	$0.4 \times 10^8$	$\sim 100$
	$0.7 \times 10^8$	$\sim 100-200$
	$1 \times 10^8$	$\sim 100-250$
	$2 \times 10^8$	$\sim 100-500$
	$3 \times 10^8$	$\sim 100-800$

ranged from 2.8 to  $13 \mu\text{s}$  with a geometric mean of  $5.6 \mu\text{s}$ . We assumed that the initial half-cycle duration is unlikely to be less than  $2.5 \mu\text{s}$  and used this as an additional criterion in determining allowed combinations of  $\Delta h$  and  $v$ .

[53] From Figure B3 one can see that the ratio of the initial field peak to the opposite polarity overshoot decreases with increasing current risetime. The ratios for current risetimes of 3, 6, and  $9 \mu\text{s}$  are 8.5, 4.0, and 2.3, respectively. For a current risetime of  $8.5 \mu\text{s}$  the ratio is 2.5, which is the minimum allowed value assumed in our study. Since we assume that the lower bound on channel length is 100 m, and increasing the channel length causes a decrease in the

**Figure B3.** (a) Currents and (b) corresponding electric fields for the same total current duration ( $30 \mu\text{s}$ ) and peak (50 kA) but different zero-to-peak risetimes of 3, 6, and  $9 \mu\text{s}$  for  $\rho = 0$ ,  $\Delta h = 100 \text{ m}$ , and  $v = 2 \times 10^8 \text{ m/s}$ .

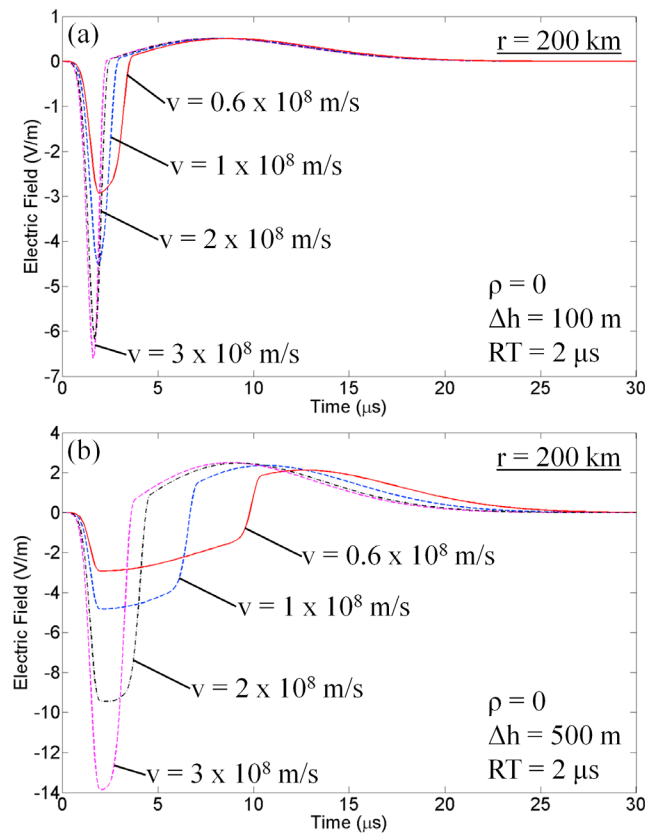


**Figure B4.** Electric field waveforms at 200 km for different propagation speeds and channel lengths of (a) 100 m and (b) 500 m, for a current risetime of 2  $\mu\text{s}$  and  $\rho = 0$ .

ratio (Figure B1), a current risetime longer than 8.5  $\mu\text{s}$  would result in an electric field waveform that is inconsistent with experimental data for any channel length equal to or greater than the lower bound, when the propagation speed is  $2 \times 10^8$  m/s. In fact, for propagation speeds of  $0.7 \times 10^8$  m/s to  $3 \times 10^8$  m/s, the ratio remains approximately 2.5 (varies from 2.47 to 2.55), when the current risetime is 8.5  $\mu\text{s}$ . Tables B2 and B3 list the allowed combinations of reflection coefficients, propagation speeds, and channel lengths that produce distant field waveforms that are consistent with experimental data for current risetimes of 3 and 2  $\mu\text{s}$ , respectively.

[54] The following criteria were used in determining allowed combinations: (1) the ratio of initial peak to opposite polarity overshoot is equal to or greater than about 2.5 (2) the total duration of initial half cycle is equal to or greater than about 2.5  $\mu\text{s}$ , and (3) the overall shape of the initial half cycle is consistent with observed ones. For longer risetimes, the domain of allowed  $\Delta h$ - $v$  combinations was determined by the ratio (criterion 1). For short risetimes and shorter channel lengths, the domain of allowed  $\Delta h$ - $v$  combinations was determined by the total duration of the initial half cycle (criterion 2). Criterion 3 was the primary one for short risetimes and longer channel lengths. In this latter case, the initial half cycle exhibited flattening (see Figure B4b) that is not consistent with experimental data, for all speeds other than the speed of light. Note that for a current risetime

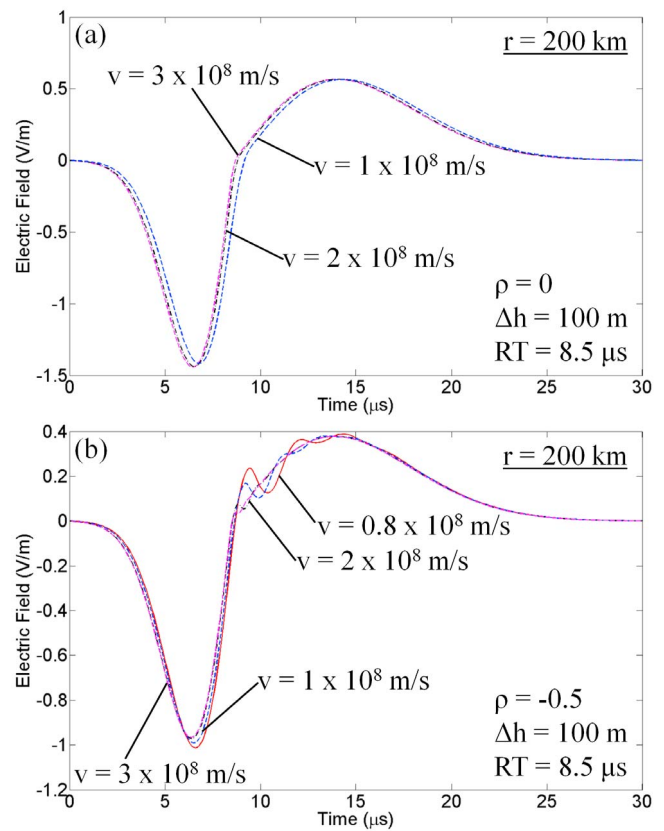


**Figure B5.** (a) Electric field waveforms at 200 km for different combinations of propagation speed and channel length for a current risetime of 8.5  $\mu\text{s}$  and  $\rho = 0$ . (b) Same as in Figure B5a but for  $\rho = -0.5$ .

of 2  $\mu\text{s}$  and  $\rho = -0.5$ , no combination of parameters produced waveforms consistent with experimental data.

[55] Transformations of distant electric field waveforms due to variations in  $\Delta h$  and  $v$  for current risetimes of 2 and 8.5  $\mu\text{s}$  are illustrated in Figures B4 and B5, respectively. Figures B4a and B4b show, for  $\Delta h = 100$  m (the lower bound on channel length, see Table B3) and  $\Delta h = 500$  m (the upper bound on channel length, see Table B3), respectively, the model predicted electric fields at 200 km (the source current is described in section 5 and shown in Figure 3a) for different propagation speeds and  $\rho = 0$ . For  $\Delta h = 100$  m, one can see that electric field waveforms for all propagation speeds, except for  $3 \times 10^8$  m/s (which violates criterion 2 described above), appear to be consistent with

**Table B3.** Combinations of Propagation Speeds and Channel Lengths That Produce Distant CID Electric Fields That are Consistent With Experimental Data for  $\rho = 0$  and Current Risetime of 2  $\mu\text{s}$ <sup>a</sup>

Current Wave Speed (m/s)	Channel Length (m)
$0.6 \times 10^8$	~100
$0.7 \times 10^8$	~100–125
$1 \times 10^8$	~100–200
$2 \times 10^8$	~100–300
$3 \times 10^8$	~200–500

<sup>a</sup>No combination produced waveforms consistent with experimental data for  $\rho = -0.5$ .

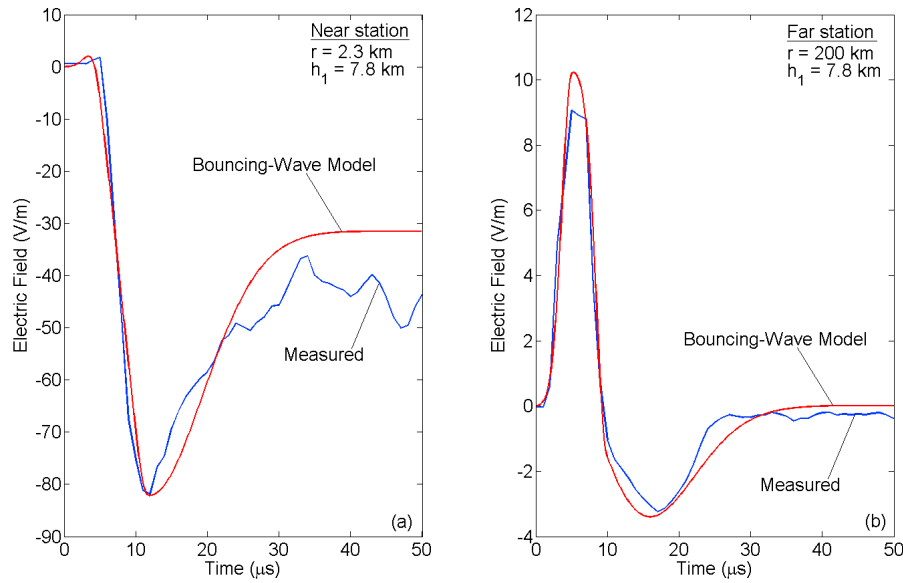


**Figure C1.** Electric fields computed using the bouncing-wave model (in red) overlaid with the fields measured by *Eack* [2004, Figure 1] (in blue) at (a) near and (b) far distances.

experimental data. However, the electric field waveforms for the upper bound on channel length ( $\Delta h = 500$  m) are inconsistent with experimental data (violate criterion 3) for all propagation speeds, except for  $3 \times 10^8$  m/s. For a current risetime of  $8.5 \mu\text{s}$ , electric field waveforms for  $\rho = 0$  (Figure B5a) and  $-0.5$  (Figure B5b) appear to be consistent with experimental data for propagation speeds ranging from about  $10^8$  to  $3 \times 10^8$  m/s only for  $\Delta h = 100$  m.

### Appendix C: Testing the Validity of Bouncing-Wave Model and Hertzian Dipole Approximation Using Electric Fields Simultaneously Measured at Near and Far Distances by *Eack* [2004]

#### C1. Bouncing-Wave Model

[56] Here, we use the simultaneously measured near and far electric field signatures of one CID reported by *Eack* [2004] to test the validity of bouncing-wave model. This same event was previously used for testing the validity of other models by *Watson and Marshall* [2007]. The CID transferred negative charge upward (or positive charge downward). We use the trial and error approach to determine a combination of CID parameters, including the current peak, the current zero-to-peak risetime (RT), the propagation speed ( $v$ ), current reflection coefficient ( $\rho$ ), and the channel length ( $\Delta h$ ), for which the bouncing-wave model predicted electric fields best match the measured electric fields at both near and far distances from the discharge. The CID channel was assumed to be vertical.

[57] Electric field signatures of this CID, measured at Los Alamos (near station) and Socorro (far station), New Mexico, are shown in Figure 1 of *Eack* [2004] and reproduced in Figure C1 of this paper. Horizontal distances were estimated, using Los Alamos Sferic Array (LASA) measurements and a time-of-arrival (TOA) method, to be 2.8 km from the Los Alamos station and about 200 km from the

Socorro station with a stated error of  $\pm 2$  km. The CID height was estimated to be 11.6 km above mean sea level. The height above local terrain should be smaller by about 2 km [*Smith et al.*, 2004]; that is, about 9.6 km. The CID height was estimated by measuring delays of ionosphere and ground-ionosphere reflections with respect to direct-path wave in VLF/LF ground-based (LASA) field records. *Smith et al.* [2004] estimated errors of this method relative to another, more accurate method that employed FORTE satellite VHF records showing direct-path and ground-reflection signals. The ground-based estimates were on average 1 km higher than the satellite estimates. After removal of the 1 km bias, the LASA height estimates were within  $\pm 1$  km of satellite estimates. Thus, the height of the CID in question is  $9.6 - 1 = 8.6$  km with a random error of  $\pm 1$  km. In summary, uncertainties in distance from the Los Alamos and Socorro stations of the CID in question are 0.8 to 4.8 km and 198 to 202 km, respectively, and uncertainties in height are 7.6 to 9.6 km above ground level. We include these uncertainties in our search for CID parameters that provide best match between model-predicted and measured electric field waveforms at both near and far distances.

[58] Figures C1a and C1b show the model predicted electric fields overlaid with the measured ones at near and far distances, respectively. A reasonably good match between calculated and measured fields was obtained for a peak current of 75 kA, total current pulse duration of  $36 \mu\text{s}$ ,  $\text{RT} = 5.2 \mu\text{s}$ ,  $v = 1.4 \times 10^8$  m/s,  $\rho = 0$ ,  $\Delta h = 650$  m, horizontal distances of 2.3 and 200 km from the near and far stations, respectively, and the height of the bottom of the CID channel of 7.8 km above ground level. The CID current pulse was assumed to be injected at the bottom end of the CID channel and to travel upward. The expression for the current waveform is given in Appendix B (equation (B1)). The values of  $g$  and  $k$  (parameters that control the shape of the current pulse) along with the best fit values of peak current, RT,  $v$ ,  $\rho$ , and  $\Delta h$  are given in Table C1.

**Table C1.** CID Parameters for Which Electric Fields Predicted by the Bouncing-Wave Model and Hertzian Dipole Approximation Best Match the Fields Measured at Near and Far Distances by *Eack* [2004]

Parameters	Bouncing-Wave Model		Hertzian Dipole Approximation	
	Best Fit Value	Allowed Range	Best Fit Value	Allowed Range
Peak current, kA	75	-	74	-
Zero-to-peak current risetime, $\mu\text{s}$	5.2	2.5–8.5 <sup>a</sup>	9	-
Total current duration ( $t_2$ ), $\mu\text{s}$	36	-	36	-
g (see equation (B1))	$18.1/t_2$	-	$10.25/t_2$	-
k (see equation (B1))	5.92	-	3	-
Propagation speed, m/s	$1.4 \times 10^8$	$0.3\text{--}3 \times 10^8$	Not applicable	Not applicable
Current reflection coefficient	0	-0.5 – 0	Not applicable	Not applicable
Channel length, m	650	100–1000	500	100 – 550
Distance from near station, km	2.3	0.8–4.8	2.4	0.8–4.8
Distance from far station, km	200	198–202	200	198–202
Height of the channel above ground, km	7.8 (lower end)	7.6–9.6	7.2	7.6–9.6

<sup>a</sup>Typical range.

## C2. Hertzian Dipole Approximation

[59] Here, we use the two-station data of *Eack* [2004] to test the validity of the vertical Hertzian dipole approximation. In contrast with the bouncing-wave model,  $v$  and  $\rho$  are not parameters of the Hertzian dipole approximation. The testing procedure used here is similar to that described above for the bouncing-wave model.

[60] Figure C2 shows electric fields based on the Hertzian dipole approximation overlaid with the fields measured at near and far distances by *Eack* [2004]. A reasonably good match between calculated and measured fields was obtained for a peak current of 74 kA, total current pulse duration of 36  $\mu\text{s}$ , RT = 9  $\mu\text{s}$ ,  $\Delta h = 500$  m, horizontal distances of 2.4 and 200 km from the near and far stations, respectively, and the height of CID channel of 7.2 km above ground level. The expression for the injected current waveform is given in Appendix B (equation (B1)), with the values of g and k along with the best fit peak current, RT, and  $\Delta h$  being given in Table C1.

## C3. Discussion

[61] The current pulse that we used for testing the Hertzian dipole approximation is the same as that employed by *Watson and Marshall* [2007] for modeling the same CID. They were unable to obtain a good match with *Eack*'s [2004] near field data using the transmission line model and assuming that the stated horizontal distance, 2.8 km, is exact. As shown in this Appendix, both the close and distant fields can be reasonably well reproduced by the bouncing-wave model (which for  $\rho = 0$  reduces to the transmission line model used by *Watson and Marshall* [2007]) when the uncertainties in the estimated horizontal distances and source height are taken into account.

[62] We now compare, with reference to Table C1, parameters for which predictions of the bouncing-wave model and Hertzian dipole approximation best match the two-station data of *Eack* [2004]. The channel lengths that fit *Eack*'s two-station data for the bouncing-wave model and Hertzian dipole approximation are similar, 650 m and 500 m,

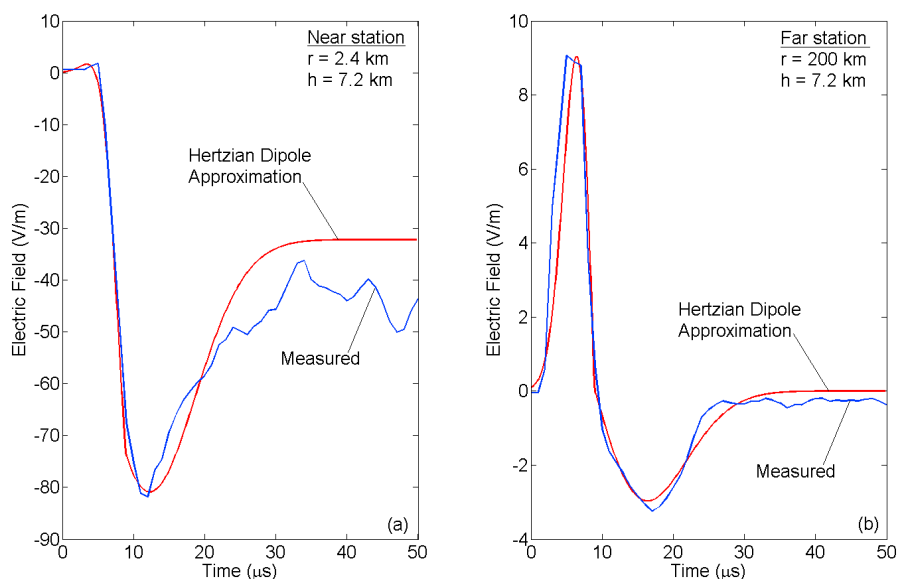


**Figure C2.** Electric fields computed using the Hertzian dipole approximation (in red) overlaid with the fields measured by *Eack* [2004, Figure 1] (in blue) at (a) near and (b) far distances.

respectively, and both are within the corresponding allowed ranges. The peak currents predicted by both models are almost the same (75 kA for the bouncing-wave model and 74 kA for the Hertzian dipole approximation). Note that our peak-current estimates of 74–75 kA are similar to that (74 kA) of *Watson and Marshall* [2007] (based on the TL model) and appreciably higher than that (29 kA) of *Eack* (based on the assumption that the near field peak is due to induction field component only). Our predicted zero-to-peak current risetime of 9  $\mu$ s for the Hertzian dipole approximation is larger than that (5.2  $\mu$ s) for the bouncing-wave model. The source heights for which a reasonably good match with two-station data is obtained for the bouncing-wave model and Hertzian dipole approximation are similar, 7.8 and 7.2 km, respectively, although the latter is slightly outside the range of uncertainty (7.6–9.6 km) in this parameter.

[63] **Acknowledgments.** The authors would like to thank D. Tsalikis for his help in developing instrumentation and acquiring experimental data and K. Eack for providing his two-station CID electric field records. This research was supported in part by NSF grants ATM-0346164 and ATM-0852869 and by DARPA.

## References

- Dwyer, J. R., M. A. Uman, and H. K. Rassoul (2009), Remote measurements of thundercloud electrostatic fields, *J. Geophys. Res.*, *114*, D09208, doi:10.1029/2008JD011386.
- Eack, K. B. (2004), Electrical characteristics of narrow bipolar events, *Geophys. Res. Lett.*, *31*, L20102, doi:10.1029/2004GL021117.
- Gurevich, A. V., and K. P. Zybin (2004), High energy cosmic ray particles and the most powerful discharges in thunderstorm atmosphere, *Phys. Lett. A*, *329*, 341–347, doi:10.1016/j.physleta.2004.06.094.
- Gurevich, A. V., Y. V. Medvedev, and K. P. Zybin (2004), New type discharge generated in thunderclouds by joint action of runaway breakdown and extensive atmospheric shower, *Phys. Lett. A*, *329*, 348–361, doi:10.1016/j.physleta.2004.06.099.
- Hamlin, T., T. E. Light, X. M. Shao, K. B. Eack, and J. D. Harlin (2007), Estimating lightning channel characteristics of positive narrow bipolar events using intrachannel current reflection signatures, *J. Geophys. Res.*, *112*, D14108, doi:10.1029/2007JD008471.
- Krehbiel, P. R., J. A. Rioussset, V. P. Pasko, R. J. Thomas, W. Rison, M. A. Stanley, and H. E. Edens (2008), Upward electrical discharges from thunderstorms, *Nat. Geosci.*, *1*, 233–237, doi:10.1038/ngeo162.
- Le Vine, D. M. (1980), Sources of the strongest RF radiation from lightning, *J. Geophys. Res.*, *85*, 4091–4095, doi:10.1029/JC085iC07p04091.
- Nag, A., and V. A. Rakov (2010), Compact intracloud lightning discharges: 2. Estimation of electrical parameters, *J. Geophys. Res.*, *115*, D20103, doi:10.1029/2010JD014237.
- Nag, A., V. A. Rakov, D. Tsalikis, and J. A. Cramer (2010), On phenomenology of compact intracloud lightning discharges, *J. Geophys. Res.*, *115*, D14115, doi:10.1029/2009JD012957.
- Rakov, V. A., and M. A. Uman (2003), *Lightning: Physics and Effects*, Cambridge Univ. Press, New York.
- Rison, W., R. Thomas, P. Krehbiel, T. Hamlin, and J. Harlin (1999), A GPS-based three-dimensional lightning mapping system: Initial observations in central New Mexico, *Geophys. Res. Lett.*, *26*(23), 3573–3576, doi:10.1029/1999GL010856.
- Smith, D. A. (1998), Compact intracloud discharges, Ph.D. dissertation, Univ. of Colo. at Boulder, Boulder.
- Smith, D. A., X. M. Shao, D. N. Holden, C. T. Rhodes, M. Brook, P. R. Krehbiel, M. Stanley, W. Rison, and R. J. Thomas (1999), A distinct class of isolated intracloud discharges and their associated radio emissions, *J. Geophys. Res.*, *104*, 4189–4212, doi:10.1029/1998JD200045.
- Smith, D. A., M. J. Heavner, A. R. Jacobson, X. M. Shao, R. S. Massey, R. J. Sheldon, and K. C. Wiens (2004), A method for determining intracloud lightning and ionospheric heights from VLF/LF electric field records, *Radio Sci.*, *39*, RS1010, doi:10.1029/2002RS002790.
- Solomon, R., V. Schroeder, and M. B. Baker (2001), Lightning initiation-conventional and runaway-breakdown hypotheses, *Q. J. R. Meteorol. Soc.*, *127*, 2683–2704.
- Thomas, R., P. Krehbiel, W. Rison, T. Hamlin, J. Harlin, and D. Shown (2001), Observations of VHF source powers radiated by lightning, *Geophys. Res. Lett.*, *28*(1), 143–146, doi:10.1029/2000GL011464.
- Thottappillil, R., V. Rakov, and M. Uman (1997), Distribution of charge along the lightning channel: Relation to remote electric and magnetic fields and to return-stroke models, *J. Geophys. Res.*, *102*(D6), 6987–7006.
- Tierney, H. E., R. A. Roussel-Dupr e, E. M. D. Symbalisty, and W. H. Beasley (2005), Radio frequency emissions from a runaway electron avalanche model compared with intense, transient signals from thunderstorms, *J. Geophys. Res.*, *110*, D12109, doi:10.1029/2004JD005381.
- Uman, M. A. (1987), *The Lightning Discharge*, Academic, San Diego, Calif.
- Uman, M. A., D. K. McLain, and E. P. Krider (1975), The electromagnetic radiation from a finite antenna, *Am. J. Phys.*, *43*, 33–38, doi:10.1119/1.10027.
- Watson, S. S., and T. C. Marshall (2007), Current propagation model for a narrow bipolar pulse, *Geophys. Res. Lett.*, *34*, L04816, doi:10.1029/2006GL027426.
- Wiens, K. C., T. Hamlin, J. Harlin, and D. M. Suszcynsky (2008), Relationships among narrow bipolar events, “total” lightning, and radar-inferred convective strength in Great Plains thunderstorms, *J. Geophys. Res.*, *113*, D05201, doi:10.1029/2007JD009400.
- Willett, J. C., J. C. Bailey, and E. P. Krider (1989), A class of unusual lightning electric field waveforms with very strong high-frequency radiation, *J. Geophys. Res.*, *94*, 16,255–16,267, doi:10.1029/JD094iD13p16255.

A. Nag and V. A. Rakov, Department of Electrical and Computer Engineering, University of Florida, 553 Engineering Bldg. 33, PO Box 116130, Gainesville, FL 32611-6130, USA. (amitabh@ufl.edu; rakov@ece.ufl.edu)